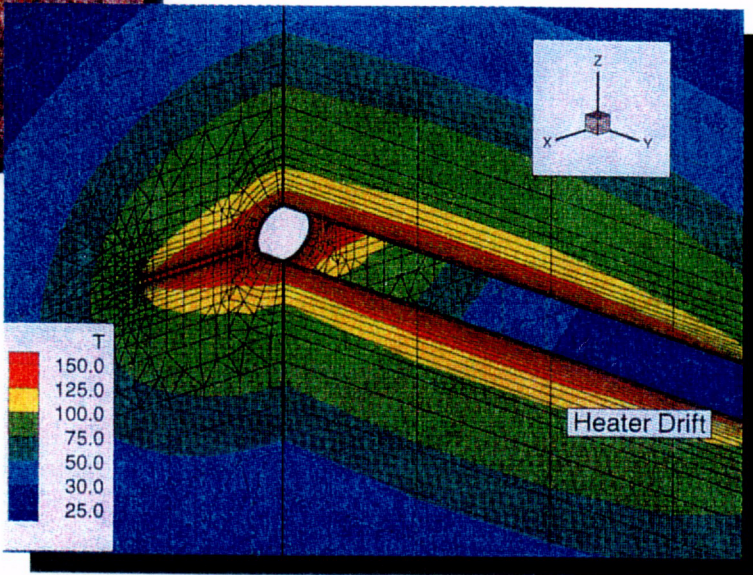
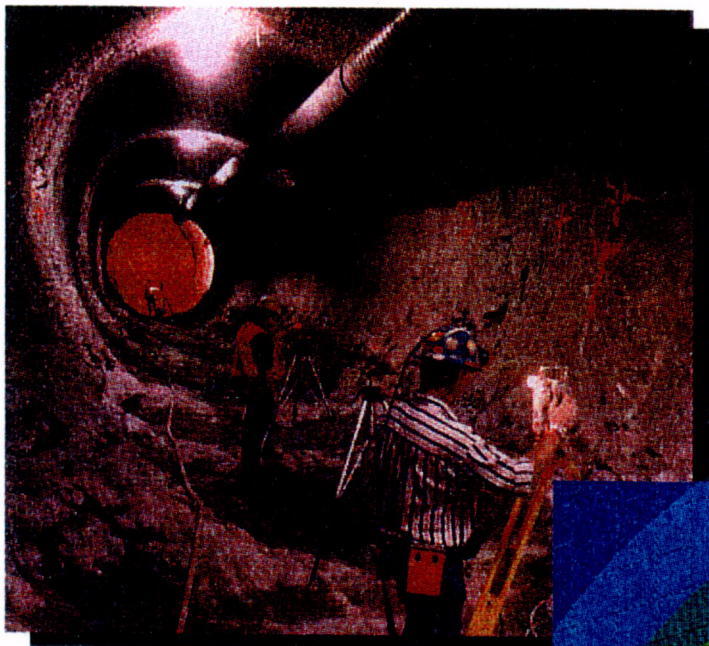


**This contractor document was prepared for the U.S. Department of Energy (DOE), but has not undergone programmatic, policy, or publication review, and is provided for information only. The document provides preliminary information that may change based on new information or analysis, and is not intended for publication or wide distribution; it is a lower level contractor document that may or may not directly contribute to a published DOE report. Although this document has undergone technical reviews at the contractor organization, it has not undergone a DOE policy review. Therefore, the views and opinions of authors expressed do not necessarily state or reflect those of the DOE. However, in the interest of the rapid transfer of information, we are providing this document for your information.**

# PRETEST ANALYSIS OF THE THERMAL-HYDROLOGICAL CONDITIONS OF THE ESF DRIFT SCALE TEST



By:

J.T. BIRKHOEZER  
Y.W. TSANG

EARTH SCIENCES DIVISION

LEVEL 4 MILESTONE SP9322M4

JUNE 1997



ERNEST ORLANDO LAWRENCE  
BERKELEY NATIONAL LABORATORY  
EARTH SCIENCES DIVISION  
1 CYCLOTRON ROAD, MAILSTOP 90-1116  
BERKELEY, CA 94720

C-01

---

## Table of Contents

1	Introduction .....	1
2	QA Status of Work.....	4
3	Problem Definition.....	5
3.1	Drift Scale Test Configuration .....	5
3.2	Conceptual Model .....	7
4	Model Concepts, Assumption and Parameters .....	11
4.1	Model Domain.....	11
4.2	Grid Design .....	12
4.3	Model Parameters.....	16
4.4	Boundary and Initial Conditions .....	21
5	Three-dimensional Thermal-Hydrological Simulation Results .....	23
5.1	Simulations Results for an Infiltration Rate of 3.6 mm/yr.....	24
5.2	Simulations Results for an Infiltration Rate of 0.36 mm/yr.....	30
5.3	Summary .....	34
6	Sensitivity Studies.....	36
6.1	Heating Schedule.....	36
6.2	Dual Permeability.....	38
7	Prediction of Sensor Readings in Hydrology Holes .....	42
7.1	Passive Monitoring.....	43
7.2	Active Testing .....	45
8	Summary .....	48
	Acknowledgments.....	49
	References .....	49
	Figures .....	F-1
	Appendix A1 .....	A1-1
	Appendix A2 .....	A2-1

simulations presented here. The SHT and DST are expected to provide the majority of site-specific data on heat-driven near-field processes in the License Application time frame.

The most prominent thermal-hydrological response of the rock mass to the heater power output is the drying of the rock mass surrounding the heat source, the carrying away of moisture in the form of vapor from the heated area, and the subsequent condensation of the vapor in the cooler regions of the rock mass farther away from the heat source. After the heat source is removed and the rock mass starts to cool off, rewetting occurs as water moves back to the vicinity of the heaters. To ensure that a large enough volume of water is heated to above boiling, and that the dominant drift-scale thermal-hydrological processes expected in a repository can be monitored in the DST within a reasonable time frame, the DST has both canister heaters that will heat up the entire length (47.5 m) of the drift and wing heaters emplaced in 50 boreholes, orthogonal to and flanking the Heater Drift. The power of all canister and wing heaters can be varied within its full range. One objective for the pre-test calculations in this report is to provide input for arriving at an appropriate heating schedule for the DST. One main criterion governing the heating schedule is based on one of the thermal goals of the repository design, namely that the temperatures at the drift wall should not exceed 200 °C.

To monitor the thermal-hydrological evolution in the DST test block, various measuring systems will be installed in boreholes drilled from the Heater Drift, as well as from the Observation Drift parallel to the Heater Drift. In particular, there are twelve "hydrology holes," 40 m in length, and in three arrays of 5, 5 and 2 boreholes drilled from the Observation Drift. Each of these arrays of hydrology holes forms a fan in a plane orthogonal to the Heater Drift and brackets it. Each hydrology hole will be segregated by high-temperature inflatable packers into four zones, and each zone will be instrumented with sensors to monitor the temperature, relative humidity, and pressure. In addition to passive monitoring, active testing will be performed. This involves the injection of air in the individual zone isolated by packers, and the monitoring of the pressure response in all other packed zones in the hydrology holes, at different stages of the DST. These tests will help in understanding how the gas-phase permeability of the rock changes in time during heating and cooling, and in turn delineate the time evolution of the condensation zones. In this report's presentation of DST simulated results, particular attention will be paid to the predictions of the readings of the sensors in the twelve hydrology holes.

The numerical simulations presented in this report are performed in three dimensions with the multi-component, multi-phase flow simulator TOUGH2 (Pruess, 1987 and 1991; Pruess et al., 1996; Wu et al., 1996). The configuration, parameters, and initial and boundary conditions of the numerical model developed in this study are designed to resemble the Drift Scale Test as closely as possible. Furthermore, all site-specific characterization data such as laboratory measurements of thermal and hydrological properties of cores from the Drift Scale Test block, *in-situ* air permeability characterization, and borehole video logs are incorporated into the

## 2 QA Status of Work

The work performed in this study is documented in Yucca Mountain Project Scientific Notebook YMP-LBNL-JBH-2. For input to this study, LBNL has used data collected under an approved YMP QMP. The software packages used in this study include standard spreadsheets and visualization and plotting programs. Such programs are not subject to QA requirements under QARD Rev. 7. The software used to simulate thermal-hydrological conditions in the Drift Scale Test with effective continuum and dual permeability formulation is the TOUGH2 code (Pruess, 1987, 1991). This program has been qualified under an approved YMP QAP (Pruess et al., 1996; Wu et al., 1996). Inversion is performed with the qualified calibration code ITOUGH2 (Finsterle, 1993; Finsterle et al., 1996).

The conclusions of this report are mainly based on qualified data and qualified software. The data used for the 1-D SD-9 calibration are Q, as are most of the additional hydrological and thermal data needed for the DST model. Site-specific data of the thermal testing area are incorporated whenever possible, and are mostly Q. The stratigraphic layering at the DST is based on the UZ site-scale flow model, and is non-Q (Bodvarsson et al., 1997). All data on the specific geometry of the drift scale test configuration, including the borehole configuration, are non-Q. The DST is still under construction, and therefore the geometry used in the model represents design coordinates, not as-built coordinates.

while the far end of the outer heater is located at the bottom of the boreholes, 11.5 m from the drift wall. The wing heaters are represented by the shaded area in Figure 3.1-1. The maximum power of each wing heater is 1.145 KW for the inner part and 1.716 KW for the outer part. The power can be regulated in 5% intervals; however, the 2/3 power ratio between inner and outer heater must be maintained. Altogether, the in-drift heaters have a total maximum power of 67.5 KW, while the 50 wing heaters have a total maximum power of 143.05 KW.

Numerous sensors are installed in over 80 instrument boreholes in the DST to monitor the thermal, mechanical, hydrological, and chemical responses of the test. Radial arrays of 20 m long boreholes intended for closely spaced temperature sensors are drilled from the Heater Drift. Similar radial arrays of shorter boreholes (15 m in length) are located along the Heater Drift for monitoring mechanical rock displacement. Four long boreholes, drilled from the Connecting Drift and parallel to the Heater Drift, are designed for measuring temperature and rock mass displacement. There are also three horizontal boreholes, drilled from the Observation Drift towards the Heater Drift, for measuring displacement. The other 36 boreholes that originate from the Observation Drift are oriented south/north toward the Heater Drift and have incline angles ranging from +24° to -22° from the horizontal, so that different rock portions above and below the Heater Drift are covered. They are all 40 m in length and form spatial clusters of two to five boreholes. These clusters of boreholes serve different purposes. Ten boreholes are designed for moisture measurements with neutron probes, four boreholes are designed for performing electrical resistivity tomography measurements, ten boreholes are designed for chemical analysis, and twelve boreholes are particularly designed for capturing thermal-hydrological behavior ("hydrology holes").

The hydrology holes will be installed with high-temperature packers, high-temperature pressure transducers, and humicaps that measure both the relative humidity and the temperature. They are arranged in three arrays of 5, 5 and 2 boreholes. hydrology holes 57, 58, 59, 60 and 61 are located at  $y = 10.06$  m measured from the bulkhead, hydrology holes 74, 75, 76, 77 and 78 at  $y = 30.18$  m, and hydrology holes 185 and 186 at  $y = 44.8$  m, close to the western terminus of the Heater Drift. Each of these arrays forms a fan in a plane orthogonal to and brackets the Heater Drift. The borehole configuration is illustrated in Figures 3.1-2, showing cross-sections transverse to the Heater Drift axis at  $y = 10.06$  m and  $y = 30.18$  m, respectively. Table 3.1 summarizes the borehole layout of the DST.

stratigraphic units. Hydrologic properties in the UZ site-scale flow model are obtained from calibration against all available data, including liquid saturation, moisture tension, perched water, pneumatic pressures, temperature, etc. Since SD-9 is the well closest to the DST area, properties used in the DST model correspond specifically to parameters derived from calibration against data in Borehole SD-9. As site-specific characterization data are being collected in the thermal alcove, including the DST area, these will be incorporated as much as possible in our numerical model.

The percolation flux at the DST horizon has a significant impact on the thermal-hydrological response of the rock formation to the applied heat, in that a higher flux can give rise to lower temperature and a larger extent of the condensation zone. Since the percolation flux is related to the surface infiltration flux, which is one of the most uncertain parameters at Yucca Mountain, the numerical model presented here shall be exercised for two different infiltration rates - the best estimate of 3.6 mm/yr, and one only one-tenth of the expected estimate, 0.36 mm/yr - in order to include a full range of plausible responses. Infiltration is assumed to be constant in time; no episodic events are considered.

One of the key parameters in controlling the thermal-hydrological response of the welded tuff in the DST is the fracture permeability. It affects the temperature through heat convection, and it impacts the time evolution and spatial redistribution of moisture through the transport of water vapor and liquid water. Moreover, it is the gas-phase permeability that is of particular importance since the liquid-phase permeability is typically very low in the welded tuff units at ambient state. Site-specific characterization of the gas-phase permeability in the DST area was carried out (Tsang and Cook, 1997) while the Heater Drift was still under construction, and hence none of the wing heater and temperature boreholes originating from the Heater Drift were available for testing. Prior to April 1997, fourteen 40-m boreholes originating from the Observation Drift had been drilled. Each borehole was separated by three inflatable packers into approximately 12-m zones, and a pressure sensor was installed in each packed-off zone. Air injection tests were carried out in each packed-off zone, and the pressure responses in the injection zone and all monitoring zones were monitored. The steady-state pressure response in the injection zone gives the local permeability, and the interference pressure response in all monitored zone gives the connectivity characteristics. Consistent with the borehole videos, which indicate that all the boreholes are intercepted by numerous fractures, the interference air permeability data indicate that the fractures are well connected, in that pressure response is obtained in most monitoring zones. However, the magnitude of the pressure response is typically small in the monitored zones as compared to that in the injection zone, and a direct connection between two packed-off zones by a large fracture such as that found in the SHT block test (Birkholzer and Tsang, 1996) is not evidenced here.

includes the binary vapor-air diffusion rather than the enhanced vapor diffusion. The diffusion coefficient  $D_{va}$  for the vapor-air mixture in a porous medium is calculated by (Vargaftik, 1975; Walker et al., 1981)

$$D_{va} = \tau\phi S_g D_{va}^o \frac{P_o}{P} \left[ \frac{T}{T_o} \right]^\theta \quad (3.2-1)$$

Here,  $D_{va}^o$  is the free-space diffusion coefficient,  $\theta$  is a factor for temperature dependence,  $\phi$  is the porosity,  $S_g$  is the gas saturation,  $\tau$  is the tortuosity factor,  $T$  is temperature,  $P$  is pressure, and  $T_o$  and  $P_o$  are standard conditions of 0 °C and 1 bar. The parameter group  $\tau\phi S_g$  represents the reduction of diffusion strength in a porous medium and is usually on the order of 0.01.

For the modeling of the DST, the effect of vapor pressure lowering due to capillary and phase adsorption effects is included. This effect is represented by Kelvin's equation (Edlefsen and Anderson, 1943)

$$f_{vpl} = \frac{P_v(T, S_l)}{P_{sat}(T)} = \exp\left(\frac{m_l P_c(S_l)}{\rho_l R(T + 273.15)}\right), \quad (3.2-2)$$

where  $f_{vpl}$  is the vapor pressure lowering factor,  $P_v$  is vapor pressure,  $P_{sat}$  is saturated vapor pressure of bulk liquid,  $P_c$  is the difference between liquid and gas-phase pressures,  $m_l$  is the molecular weight of the liquid,  $R$  is the universal gas constant, and  $T$  is temperature in °C. The definition of the vapor pressure lowering factor  $f_{vpl}$  is identical to the definition of relative humidity. For the duration of the DST, there will be a large volume of rock in the dry-out region where the capillary pressure  $P_c$  attains a very strong negative value. The readings in the relative humidity sensor will serve to monitor the evolution of the dry-out zones in the DST.

the boundary at infinity (i.e., constant primary variables). The northern lateral boundary is 90.0 m north of the centerline of the Heater Drift; the southern lateral boundary is 90.0 m south of the centerline of the Heater Drift. The eastern lateral boundary is 90.0 m east of the hot side of the bulkhead, 88.0 m east of the cold side of the bulkhead and 74.5 m east of the Connecting Drift. The western lateral boundary is 90.0 m west of the western terminus of the Heater Drift, 137.5 m from the hot side of the bulkhead. The overall north-south extension is 180.0 m and the overall east-west extension is 227.5 m.

Table 4.1-1: Vertical Layering of the Model Domain

Geological Unit	Formation Name	Thickness (m)	Bottom Elevation		Top Elevation	
			global (m NN)	local (m)	global (in m NN)	local (m)
Topopah Spring	tptpul	85.39	1066.86	14.00	1152.25	99.39
Topopah Spring	tptpmn	40.68	1026.18	-26.68	1066.86	14.00
Topopah Spring	tptpll	130.08	896.10	-156.76	1026.18	-26.68

## 4.2 Grid Design

Grid generation is an important part of developing a complex 3-D model. The aim of grid generation is to achieve a proper balance between desired numerical accuracy and computational time, both of which are controlled by the total number of grid blocks. In the DST, the grid must be compatible with sharp gradients of temperature, saturation and pressure which may occur at different distances from the heat source as time progresses. At the same time, major hydro-geological features must be captured, and the special geometry of the test area (including tunnels, decline of the drifts and boreholes of interest) must be realistically represented. All these objectives were met by the grid designed as described in this section.

Several automatic grid generation modules have been developed to allow for accurate and efficient generation of 2-D and 3-D grids. In a first step, a 2-D vertical mesh is designed within the local xz-plane, i.e., orthogonal to the Heater Drift centerline. Local mesh refinement is particularly important in this plane, as most of the heat produced by the in-drift heaters and the wing heaters is released transverse to the Heater Drift centerline. In a second step, the complete 3-D DST grid is created by appropriately extending several vertical 2-D planes into the third

around the Heater Drift using grid generator Module 1, with radial increments as small as 0.05 m at the drift wall ( $R = 2.5$  m) increasing up to 0.80 m at a radial distance of 7.0 m. Starting from this distance, the radial symmetric mesh transforms gradually into a rectilinear mesh. Module 2 is used to generate a locally refined mesh for the rock mass close to the wing heaters, with a similar design for both sides of the drift. Increments in the vertical direction start as small as 0.05 m at the heater-rock interface, and gradually increase with distance from the heater. Module 3 is then applied to superpose the local heater grids on a less-refined larger mesh for the entire vertical cross section, also generated using Module 2. The resulting grid design is symmetrical to the z-axis, except for an area adjacent to the Observation Drift. Here, another appropriately designed subgrid has been superimposed to adapt the geometry of the drift. The resulting 2-D mesh as shown in Figure 4.1-1 has 2242 grid blocks and 5057 connections between them.

Also included in Figure 4.2-2 is the location of the 5 hydrology holes 57 through 61 which form a fan in the xz-plane, starting from the Observation Drift. Figures 4.2-3 and 4.2-4 show two other xz-cross sections, located at  $y = 30.18$  m and  $y = 44.8$  m. The figures depict the configuration of hydrology holes 74 through 78 and 185 through 186. Note that the altitude of the Observation Drift varies in the different cross sections, as the drift gradually declines from the ESF main drift towards the thermal testing area.

Altogether, 24 2-D element planes have been merged in the y-direction (along the Heater Drift axis, perpendicular to the xz-cross section shown above) to generate the entire 3-D mesh. Table 4.2-1 gives a short summary of the arrangement of the planes. Starting from  $y = 0.0$  m at the hot side of the bulkhead, planes 1 through 10 represent the heated section of the drift. The planes are arranged such that the location of hydrology holes (i.e.,  $y = 10.06$  m,  $y = 30.18$  m, and  $y = 44.8$  m) matches with the center of Planes 4, 6, and 8, respectively. Each of these 10 planes has an identical 2-D discretization, except for the location of the Observation Drift, which varies in altitude from layer to layer. The next five planes 11 through 15 extend beyond the Heater Drift up to  $y = 137.5$  m. The first four planes in negative y-direction, -1 through -4, extend along the bulkhead and the non-heated section of the Heater Drift. Plane -5 incorporates the width of the Connecting Drift (where certain grid blocks are cut-out from the original mesh to account for the open tunnel), and the remaining 3 planes extend from the Connecting Drift up to  $y = -90.0$  m. Figure 4.2-5 depicts a vertical cross section along the centerline of the Heater Drift, focusing on the thermal test area and facing approximately south in the negative x-direction. Arrows at the top indicate planes where hydrology holes exist. (Note that the displayed grid in Figure 4.2-5 does not show the actual interfaces between grid blocks in the finite difference discretization, as do Figures 4.2-1 through 4.2-4. The post-processing plotting software automatically designs a mesh by connecting the center nodes of each finite difference grid. This post-processed mesh is depicted here.)

head, which insulates the heated section of the Heater Drift, is not explicitly modeled in this study. It is assumed that the bulkhead is a perfect insulator for heat transport in the drift, allowing no heat to escape from the Heater Drift to the "cold" side. Geometrical features of minor importance for the thermal-hydrological conditions in the test area, such as the plate loading niche or the DAS/Office Niche, are not represented in the model. Also note that all xz-planes outside of the heated section of the drift are modified in the grid design; i.e. very small grid blocks are merged together with increasing distance from the heaters. The entire 3-D model grid is composed of 48,249 grid blocks and 157,474 connections between them.

### 4.3 Model Parameters

All hydrological and thermal properties presented in this section are qualified if not otherwise stated. The matrix and fracture flow properties used in the DST model are carefully calibrated using inversion techniques to match measured data from Borehole SD-9. The inversion takes a property set for the initial guess derived in current calibration efforts performed for the UZ site-scale flow model (Bandurraga and Bodvarsson, 1997). Special constraint was placed on the inversion in that site-specific data of the thermal testing area are incorporated. The calibration is performed as follows:

- The calibration procedure uses the qualified inverse modeling code ITOUGH2 (Finsterle, 1993; Finsterle et al., 1996), applied to a one-dimensional vertical column extending from the ground surface down to the water table. Steady-state conditions and constant infiltration rates are assumed. The interaction between fractures and matrix is modeled with the ECM concept.
- The calibration is performed for two different infiltration rates, 3.6 mm/yr, which is the actual infiltration rate interpolated for the location of Borehole SD-9 from the most recent infiltration map for Yucca Mountain (Flint et al., in prep.), and 0.36 mm/yr as a bounding case, since the percolation flux at the repository horizon remains one of the most uncertain data at Yucca Mountain.
- The rock properties are calibrated against measured saturation and water potential data from borehole SD-9. Calibrated parameters are permeability and van Genuchten  $\alpha$  and  $m$ , for both fractures and matrix. Input parameters for the specific calibration process for SD-9 are site average values and their standard deviation for the different layers. Input parameters for fracture and matrix permeability and the matrix van Genuchten  $\alpha$  and  $m$  are based on laboratory and field measurements. Since no measurements exist for the fracture van Genuchten parameters, reasonable values have to be estimated. (See details in Sonnenthal et al., 1997).
- Some of the most sensitive parameters that will dictate the thermal-hydrological conditions of the Drift Scale Test are thermal conductivity, fracture gas-phase per-

enough to allow for a non-equilibrium of capillary pressure throughout the entire Topopah Spring unit. If this is the case, the inversion procedure for liquid flow in the unsaturated zone should be modeled using a dual permeability model (DKM), with possibly reduced fracture-matrix interaction (Doughty and Bodvarsson, 1997; Bandurraga and Bodvarsson, 1997; Ho, 1997), which will give rise to a different set of parameters. For this study we rely exclusively on the inversion parameters from the ECM conceptualization for material properties and initial conditions.

Table 4.3-1: Calibrated parameters for the DST model layers

<b>Fracture Permeability (m<sup>2</sup>)</b>	<b>Infiltration 3.6 mm/yr</b>	<b>Infiltration 0.36 mm/yr</b>
tptpul	0.202 10 <sup>-11</sup>	0.635 10 <sup>-12</sup>
tptpmn	0.100 10 <sup>-12</sup> *	0.100 10 <sup>-12</sup> *
tptpll	0.1554 10 <sup>-11</sup>	0.187 10 <sup>-11</sup>
<b>Matrix Permeability (m<sup>2</sup>)</b>		
tptpul	0.200 10 <sup>-16</sup>	0.525 10 <sup>-17</sup>
tptpmn	0.914 10 <sup>-17</sup>	0.124 10 <sup>-16</sup>
tptpll	0.233 10 <sup>-16</sup>	0.247 10 <sup>-15</sup>
<b>Fracture van Genuchten α (1/Pa)</b>		
tptpul	0.314 10 <sup>-4</sup>	0.157 10 <sup>-3</sup>
tptpmn	0.217 10 <sup>-4</sup>	0.973 10 <sup>-4</sup>
tptpll	0.234 10 <sup>-4</sup>	0.166 10 <sup>-4</sup>
<b>Matrix van Genuchten α (1/Pa)</b>		
tptpul	0.611 10 <sup>-5</sup>	0.106 10 <sup>-4</sup>
tptpmn	0.171 10 <sup>-5</sup>	0.225 10 <sup>-5</sup>
tptpll	0.335 10 <sup>-5</sup>	0.282 10 <sup>-5</sup>
<b>Fracture van Genuchten m</b>		
tptpul	0.492	0.492
tptpmn	0.483	0.492
tptpll	0.492	0.492
<b>Matrix van Genuchten m</b>		
tptpul	0.252	0.243
tptpmn	0.320	0.247
tptpll	0.229	0.207

\* parameter "fixed" in calibration

measurements by REKA probe in the DST area give a thermal conductivity of about 2 W/(m °K) (R. Datta, personal communication, non-Q), which is consistent with the core sample measurements, since the ambient matrix saturation in the DST is quite high. For the other layers, recent estimates are used from core samples from North Ramp boreholes (Brodsky et al., 1997). Values for heat capacity are used as given in DOE/RIB (1993). Rock particle density is used instead of rock grain density; values are taken from Flint et al. (in prep.). Differences in particle and grain density at Yucca Mountain are generally smaller than 1%, however, they could be more relevant in lithophysal zones where cavities exist. Also, thermal conductivity may be overestimated in lithophysal zones because the measurements are based on recovered cores, so that large non-interconnected pore space is not considered.

Reasonable numbers for the vapor diffusion parameters are  $D_{va}^0 = 2.14 \times 10^{-5} \text{ m}^2/\text{s}$  and  $\theta = 2.334$ , after Pruess and Tsang (1994). A reasonable number for the tortuosity of the path followed during the gas diffusion process is  $\tau = 0.2$ . These parameters are non-Q, as no measurements exist; however, the effect of binary vapor-air diffusion is very small compared other thermal-hydrological processes. This would change only when enhanced vapor diffusion was considered, and the parameter group  $\tau\phi S_g$ , here on the order of 0.01, was significantly increased by several orders of magnitude. In the present study for the DST, binary vapor-air diffusion is considered rather than enhanced vapor diffusion (see discussion in Section 3.2 above).

Table 4.3-2 Hydrogeological and thermal input values

Parameter	tptpul	tptpmn	tptpll
Matrix Porosity	0.154	0.11	0.13
Matrix Residual Liquid Saturation	0.06	0.18	0.08
Rock Particle Density in kg/m <sup>3</sup>	2510.0	2530.0	2540.0
Fracture Porosity	0.000171	0.000263	0.000329
Fracture Residual Liquid Saturation	0.01	0.01	0.01
Rock Thermal Conductivity in W/(m °K) ("wet")	1.7	2.0	2.29
Rock Thermal Conductivity in W/(m °K) ("dry")	1.15	1.67	1.59
Rock Mass Heat Capacity in J/(kg °K)	916.7	952.9	952.9
Vapor Diffusion Coefficient in m <sup>2</sup> /s	$2.14 \times 10^{-5}$	$2.14 \times 10^{-5}$	$2.14 \times 10^{-5}$
Factor for Temperature Dependence	2.334	2.334	2.334
Tortuosity	$\tau = 0.2$	$\tau = 0.2$	$\tau = 0.2$

thermal conductivity material. In this model, the non-heated section of the Heater Drift is assumed to be completely insulated, while the Connection and Observation Drift is assumed to be insulated on the near-heater walls only. The insulation is explicitly modeled, it is 15.2 cm thick, has a 0.0447 Watt/(m<sup>2</sup> K) thermal conductivity, a density of 32 kg/m<sup>3</sup>, and a heat capacity of 835 J/(kg K) (values chosen are similar to the SHT-design calculations, Birkholzer and Tsang, 1996). The surfaces are assumed to be open for moisture to escape from the test block in the form of both liquid water and vapor.

The radiative heat exchange within the Heater Drift is not explicitly modeled in this study. The heat load generated inside the drift is placed directly onto the rock elements adjacent to the drift wall. Since it is not yet clear if the radiation in the drift is effective enough to completely equilibrate the temperature along the drift wall, two extreme cases of drift wall boundary conditions are studied to bound the effect of thermal radiation: In the first case, a *uniform areal heat load* is introduced at the rock surfaces along the drift wall, which will eventually give rise to cooler temperatures at the two ends of the Heater Drift. In the second case, a *uniform temperature* is assumed at the rock surfaces along the entire length of the Heater Drift. The first case represents a less effective radiative heat exchange within the drift, and the second case represents totally effective black body radiation within the drift. The real system behavior is expected to be bounded somewhere between the two cases. The wing heaters are modeled as two horizontal smeared-out heat sources on either side of the drift. Assuming that the inner and outer wing heater sections are each 4.75 m in length and that the heat input is uniformly distributed along the 47.5-m-long heated portion of the drift, the areal horizontal load amounts to a maximum of 126.9 KW/m<sup>2</sup> of the inner wing heater and 190.1 KW/m<sup>2</sup> for the outer wing heater. It is assumed that no thermal radiation takes place between the wing heater boreholes and the Heater Drift; i.e., the temperature in the wing heaters is not necessarily in equilibrium with the drift temperature.

Figures 4.4-1 and 4.4-2 present the initial thermal-hydrological situation in the 3-D DST model domain for the 3.6 mm/yr and the 0.36 mm/yr scenario, showing matrix saturation, fracture saturation, and temperature measured along a vertical sampling line. The vertical sampling line chosen is located at  $x = 0.0$  m and  $y = 30.18$  m, and thus intersects the Heater Drift. Note a minor increase in liquid saturation above the Heater Drift, and a minor decrease below, as the percolation flux must bypass the tunnel. The fracture continuum saturations are consistently higher in the high infiltration case compared to the low infiltration case. For high infiltration rates, most of the vertical flux takes place in the fracture continuum, as the matrix is not conductive enough to support the infiltrated liquid. In fact, for the tptpmn layer the ratio of vertical flux occurring in the fractures to the entire vertical flux in the rock amounts to about 80% for the high infiltration case, but only about 1% for the low infiltration case. The temperature profile reflects the geothermal gradient.

Section 6. One of the many heating schedules analyzed in the 2-D simulations was eventually chosen as base-case for the three-dimensional runs. This heating schedule, described above, meets the 200 °C constraint for both the 3.6 mm/yr and the 0.36 mm/yr scenario. Furthermore, choosing full capacity of heating from the beginning of the test insures that within the drift wall temperature constraint, maximum heat input can be provided to the rock mass so that a larger volume of rock is heated up for a longer duration of time. The heating schedule chosen is a fairly simple scheme, and no effort was made to fine-tune or optimize the setup assuming more complex heating schedules, such as ramping down the heater power instead of just dropping from 100% to 50%, or running the in-drift and wing heaters at different percentages of their maximum capacity. We show below that the drift wall temperature is sensitive to different infiltration and heat exchange scenarios; therefore, further optimization of the heating scheme seems unnecessary for these pretest calculations. During the DST, when the model will be calibrated to field measurements, the heating schedules for the remaining test period can and will be optimized using updated simulation runs.

## 5.1 Simulation Results for an Infiltration Rate of 3.6 mm/yr

The first part of this section presents the thermal-hydrological conditions for an infiltration rate of 3.6 mm/yr and a uniform heat load applied along the walls of the Heater Drift. This gives rise to a non-uniform temperature distribution along the walls. Simulation runs using a uniform temperature boundary condition along the Heater Drift wall will be briefly discussed at the end of this section. It will be shown, however, that the choice of the heat exchange model within the Heater Drift has little effect on the thermal-hydrological response in the bulk of the rock mass.

Figure 5.1-1 through 5.1-3 show the temperature evolution in the Heater Drift at three different distances from the bulkhead, namely  $y = 10.06$  m,  $y = 30.18$  m and  $y = 44.8$  m, respectively. These three distances coincide with the location of the three arrays of hydrology holes, and represent layers 4, 6 and 8 of the 3-D model grid (see Table 4.2-1). All temperature curves are similar, and essentially reflect the heating schedule: The temperatures rise very fast in the beginning, show a minor heat-pipe effect near 100 °C, and reach a first peak after 1 year. At this time, the heater power is reduced to 50%, and the temperature at the drift wall almost instantly drops about 20 to 30 °C. Eventually, the temperature starts rising again, but much more slowly than before due to the reduced thermal load. After 4 years, the heaters are turned off, and initially the temperature in the drift decreases rapidly. At later stages, however, the cooling process slows down significantly, and the in-drift temperatures after 4 years of cooling are still as high as 70 °C. Generally, the temperature history is characterized by three stages: a rapid temperature rise in the first year, a more steady-state high-temperature “plateau” thereafter, and a cooling period in the end. The temperature response to changes of the heat power is much dampened and retarded with increasing distance from the drift wall; e.g. the temperature readings in all

stage of heating; only the very ends of the heated section show lower temperatures. This shows that the heat fluxes are mainly orthogonal to the Heater Drift centerline, and implies that a 2-D vertical model considering thermal-hydrological conditions in the xz-plane might be a good representation of the 3-D behavior at this time.

Figures 5.1-6 and 5.1-7 show the matrix liquid saturation at 1 year, which is significantly different from the initial moisture distribution presented in Figure 4.4-1 above. An extended dry-out zone has developed around the Heater Drift and the wing heaters. Moisture is carried away from the heated area in the form of vapor, mainly in the fractures because of the low matrix conductivity, and driven by the gas pressure gradient. In cooler regions, the vapor condenses at the fracture walls, giving rise to an increase in liquid saturation in both fractures and matrix. Subsequently, the liquid, driven by capillary forces, migrates away from the condensation zone; part of it towards the boiling region, and smaller amounts outward, away from the heaters. The resulting moisture distribution is clearly non-symmetrical in the vertical direction, with the majority of the saturation build-up below the heater, which indicates the presence of relatively fast gravity-driven liquid flux in the fractures. Above the heater, gravity adds to the strong capillary gradient between condensation zone and boiling area, and helps to move liquid back to the boiling region. Below the heater, gravity moves liquid away from the boiling region.

At this stage of heating, the thermal-hydrological response of the heat is limited to the tptpmn layer. The overlying tptpul layer and the underlying tptpll layer are essentially unaffected and remain at their initial saturation values of about 0.74 and 0.81, respectively. However, the saturation build-up in the tptpmn has already reached the interfaces to the adjacent geological units, and further vertical movement of the condensation zone appears to be somewhat retarded at the layer boundaries. This can be an effect of different material properties in different layers; it may also be related to the lower initial saturation in the adjacent layers, which offers a larger open matrix pore volume for the condensate. At 1 year, hydrology holes 75, 76, 77 and 78 are partially located in areas of increased matrix saturation; hydrology hole 77 is also intersecting the dry-out region below the wing heater.

Figures 5.1-8 and 5.1-9 present the liquid saturation in the fractures at 1 year. The pre-heat initial fracture saturation is about 17% in the tptpmn and about 11% in the other model layers. This saturation value is relatively high, indicating that even before turning on heat, most of the percolation flux takes place in the fracture continuum. After 1 year of heating, the fracture saturations in the tptpmn build up considerably to maximum values around 45%, which allows for significantly higher liquid fluxes in the fractures. In the condensation zone below the heater, liquid fluxes increase to about 3 m/yr in vertical downward direction, forced by gravity and capillary suction. Above and at the sides of the wing heaters, flux values are as high as 10 m/yr, driven by strong capillary forces between the condensation zone and the boiling zone. However, the increase of fracture saturation is limited by the fact that most of the condensing liquid is

The temporal evolution of the thermal-hydrological properties in the DST block requires study in more detail. Figures 5.1-22 through 5.1-25 show temperature, gas pressure, matrix and fracture liquid saturation along a horizontal sampling line in the hydrology hole plane at  $y = 30.18$  m. The sampling line extends from the center of the drift at  $x = 0.0$  m,  $z = 0.0$  m along the wing heater to the Observation Drift. Results are presented at 6 months, 1 year, 2 years, 3 years, and 4 years during the heating period, and at 1 year, 2 years, 3 years, and 4 years during the cooling period.

The temperature distributions in Figure 5.1-22 show a distinct heat-pipe region throughout the heating period. This region of liquid and vapor counter-flow is evidenced by the plateau in the temperature curve near  $100$  °C. It is also evident that the temperature distribution along the first 10 m from the drift wall is fairly uniform, indicating that the operating power of the in-drift heater and the wing heater has appropriately balanced. The temperatures in this area vary only as much as  $25$  °C during the time interval from 1 year to 4 years. This implies that the chosen heating schedule gives fairly steady-state conditions for a sufficiently long time period. Further away from the heater, the temperatures rise significantly with time, and the heated rock volume increases substantially. When the heater is turned off after 4 years, the temperatures decrease rapidly in the first year, but much more slowly thereafter. Without the vaporization and subsequent condensation processes which arise in response to heating, heat-pipe effects are absent during this cooling period.

Areas of gas pressure build-up (Figure 5.1-23) correspond to the high-temperature boiling regions shown above (Figure 5.1-22). The maximum pressures are observed during the first year of heating, while the heaters are operating at 100% power. As soon as the heater power is reduced to 50%, the gas pressures drop significantly, and remain at a constant value throughout the heating period. During cooling, gas pressures return to ambient conditions almost immediately after turning off heat.

The matrix and fracture saturation profiles shown in Figures 5.2-24 and 5.2-25, respectively, demonstrate the steep gradients of moisture content at the interface between dry-out and condensation zones. Note that the horizontal sampling line runs from the Heater Drift along the wing heaters. The dry-out zone reflects the horizontal extent of the wing heater array; beyond this array, the saturation increases immediately. The single saturation peak observed at initial heating stages about 2 m away from the drift wall is due to the horizontal offset between the drift wall and the wing heaters. The highest saturations are found at 1 year; thereafter, the saturation peak values decrease slowly with time, while the saturation front moves radially outward. The cooling of the rock results in a fast decrease of the peak saturation values to approximately the initial state before turning on the heat, as part of the liquid is driven towards the dry-out zone. However, after this fast response to turning off the heat, the rewetting process becomes very

average saturation change in the boiling area from about 92% to about 18%, more than 800 cubic meters of liquid will be mobilized in the heater test.

Also included in Figure 5.1-34 is the resulting dry-out curve for the other case studied, which assumes a uniform temperature boundary in the Heater Drift rather than the uniform areal heat load boundary discussed earlier. Both cases yield very similar results, which implies that the overall thermal-hydrological conditions are rather unaffected by the mode of heat exchange within the Heater Drift. However, within and close to the drift, the different boundary conditions give rise to substantial temperature differences. Figure 5.1-35 presents the temperature evolution at the Heater Drift wall for the uniform temperature runs. A comparison with Figures 5.1-1 through 5.1-3 reveals similar characteristics in the temperature evolution, but different absolute temperature values. The maximum temperature reached at the drift wall in Figure 5.1-35 is 160 °C after 4 year. of heating. This is about 30 °C lower than the maximum temperature value observed in Figure 5.1-2, measured at the springline of the  $y = 30.18$  m cross section. However, it is about 30 °C higher than the crown drift wall temperature measured in Figure 5.1-3, which shows the temperature evolution at  $y = 44.8$  m. Generally, the uniform temperature case tends to give lower local rock temperatures in the middle section of the Heater Drift and higher local rock temperature at the ends, when compared to the uniform areal heat load case. The real system behavior is expected to be bounded somewhere between the two cases.

Figures 5.1-36 through 5.1-39 show that the impact of the drift wall boundary condition is of very local nature. The figures present temperature and matrix liquid saturation profiles along the same horizontal and vertical sampling lines as chosen before. Heavier lines give the uniform temperature results; thinner lines show the uniform heat load results. As the sampling lines are chosen at  $y = 30.18$  m, close to the center of the Heater Drift, the uniform temperature case yields less thermal load and lower rock wall temperatures than the other case. However, the differences between the two cases decrease with increasing distance from the drift wall. In fact, with respect to the sensor readings in the hydrology holes, these differences will be marginal and can safely be neglected. Input parameter uncertainties will affect the simulation results much more than the choice of the boundary condition.

## **5.2 Simulation Results for an Infiltration Rate of 0.36 mm/yr**

In this section, additional model calculations are presented assuming an infiltration rate of 0.36 mm/yr, which is 10% of the current estimate of 3.6 mm/yr at Borehole SD-9. The surface infiltration rate is one of the most uncertain parameters at Yucca Mountain; yet it is closely related to the vertical flux through the mountain, one of the most crucial properties for the performance of the potential nuclear waste repository. The assumed percolation flux will also affect the thermal-hydrological conditions at the DST. A smaller flux rate will result in higher temperatures, since less water is seeping downward towards the heated rock volume. Another

liquid saturation in the tptpmn is almost identical for the two scenarios, as the calibration had been conditioned to a 92% saturation value.

The impact of the thermal load is immediately obvious in that a distinct dry-out zone has developed around the heaters, followed by a condensation zone featuring a substantial saturation build-up in both the matrix and the fractures. Comparison of the two infiltration scenarios shows that the dry-out is larger when the infiltration rate is low. Consequently, as more vapor is produced in a given time period, the saturation build-up in the condensation zone is more pronounced than in the 3.6 mm/yr infiltration scenario; in fact, the matrix saturation values rise up to almost full saturation. Part of the reason for this significant increase is the nature of the characteristic functions of fractures and matrix. For the low infiltration rate, the inversion yields much lower air entry pressures in the fractures than the respective values for the matrix. Consequently, the initial fracture saturation is very low; i.e., the fractures are not very conductive at ambient state. An effective mechanism for redistributing the condensate can only be provided when the fracture saturations build up sufficiently to allow for liquid mobilization in the fractures. Indeed, as can be seen in the contour plots, the maximum fracture saturations are above 40% at 1 year and above 30% at 4 years. These values are directly related to significant increases of the respective matrix saturation, as the ECM formulation assumes thermodynamic equilibrium between the two components. The resulting moisture distributions are clearly non-symmetrical in vertical direction, which indicates that the fractures indeed conduct substantial amounts of liquid away from the boiling area. The maximum fracture fluxes are about 4 m/yr at 1 year and about 1.2 m/yr at 4 years in the vertical downward direction, while fluxes from the condensation to the boiling zones are as high as 8 m/yr at 1 year and 3 m/yr at 4 years. These values are similar to the fluxes measured in the high infiltration scenario. However, in the downward direction away from the heat source, the liquid does not migrate as far as in the high infiltration scenario, as the vertical extent of the saturation build-up is clearly smaller in case of low infiltration. Again, this is mainly related to the characteristic curves: As the saturation values slowly decrease with travel distance, the fractures become less and less conductive until further migration is essentially stopped. This effect is less dominant in the high infiltration scenario, where fractures are conductive even at ambient state.

Figures 5.2-16 to 5.2-21 present the thermal-hydrological situation at 8 years, which is 4 years after the heater is turned off. The rock mass around the heater has cooled substantially during this period; it eventually arrives at a maximum temperature of 75 °C, which is slightly higher than in the high infiltration scenario. The matrix saturation contours reveal a more prominent difference between the two infiltration scenarios considered. In the low infiltration scenario, the matrix saturation in the condensation zone is (after 4 years of cooling) still significantly higher than at ambient state, while in the high infiltration scenario, the saturation build-up in the condensation zone area has already vanished at this time. This again is due to the different characteristic curves assumed: In the former scenario, the fractures drain rapidly and become

starts at (and returns to) a much smaller ambient level, namely about 5%. At this saturation, the fractures are essentially non-conductive (*Figures 5.2-25, 5.2-32, 5.2-33 compared to Figures 5.1-25, 5.1-32, 5.1-33*).

The temporal evolution of the total dry-out rock volume during heating and cooling is depicted in Figure 5.2-34. In the low infiltration scenario, the dry-out volume will rise to a maximum value of more than 13,000 cubic meters after 4 years of heating. This is about 30% more than in the other scenario. After 4 years of cooling, the dry-out rock volume has decreased to about 10,000 cubic meters; i.e., more than 3,000 cubic meters of rock have been rewetted. This process is less effective than in the high infiltration scenario, where the dry-out rock volume decreases from about 11,000 cubic meters to about 6,000 cubic meters during 4 years of cooling.

Also included in Figure 5.2-34 is the resulting dry-out curve for the other 0.36 mm infiltration case studied, which assumes a uniform temperature boundary in the Heater Drift rather than a uniform areal heat load boundary as before. However, as has already been observed in Section 5.1, the thermal-hydrological conditions in the bulk of the rock mass are rather unaffected by the Heater Drift wall boundary condition. At some distance from the Heater Drift, the differences between the two cases become marginal and can be neglected (*Figures 5.2-36 through 5.2-39*). Only within and close to the Heater Drift, the different boundary conditions give rise to substantial temperature differences (*Figure 5.2-35*).

### 5.3 Summary

The expected thermal-hydrological conditions in the DST test block are briefly summarized in this section. Table 5.3-1 gives the maximum Heater Drift wall temperatures at different stages during the heating and cooling of the rock mass. Also given is the volumetric extent of the dry-out rock mass, calculated by adding up all grid block volumes which experience a significant reduction in moisture content. The scenarios considered include a 3.6 mm/yr infiltration case and a 0.36 mm/yr infiltration case, both of which have been studied using two different drift wall boundary conditions in order to capture uncertainties from the effect of heat radiation inside the Heater Drift. All scenarios assume 1-year heating at 100% power, followed by 3 years heating with 50% power before heat is finally turned off and a passive cooling period begins. The simulation runs cover 4 years of this cooling period. Some important findings are listed below:

- The chosen heater schedule meets the criteria that (1) the drift wall temperatures do not significantly exceed 200 °C, (2) the temperatures in the near-heater rock volume remain relatively unchanged for several years, so that experiments can be performed in a quasi-steady environment, and (3) a substantial rock volume is being affected by the thermal load, as is manifested in rising temperatures, drying of rock mass due to vaporization, saturation build-up due to condensation of vapor, and enhanced liquid

## 6 Sensitivity Studies

In this section, we evaluate the sensitivity of the thermal-hydrological response in the DST to (1) different heating scenarios, and (2) alternative concepts used for modeling the fracture-matrix interaction, namely the effective continuum model (ECM) and the dual permeability formulation (DKM). In order to reduce the numerical effort, we restrict the study to two dimensions, with the modeling domain chosen to be a  $xz$ -cross section perpendicular to the Heater Drift center line. The numerical simulations are again performed with the simulator TOUGH2. The 2-D grid is identical to the  $xz$ -cross section shown in Figure 4.2-3, resembling the particular geometry of the 3-D model plane located at  $y = 30.18$  m, thus representing the vertical plane of hydrology holes 74 to 78. Unless we specify otherwise, the conceptual model, input data, and boundary and initial conditions are identical to the scenario considered in the first part of Section 5.1; i.e., a 3.6 mm/yr infiltration rate is assumed, and a uniform heat load is applied along the walls of the Heater Drift. In addition to the analysis presented here, we also examined the effects of using a different gas relative permeability formulation, using a different fracture  $m$  parameter, and neglecting vapor pressure lowering, all of which proved to be of less importance.

Results from a two-dimensional model cannot exactly represent the actual three-dimensional behavior of the rock mass. However, it will be shown that the 2-D thermal-hydrological response only slightly overestimates the three-dimensional system behavior when comparing the 2-D results to those  $xz$ -cross sections of the 3-D grid which intersect the Heater Drift in the center part, e.g.  $xz$ -planes 4, 5, or 6 (see Table 4.2-1). Two-dimensional simulations in a sensitivity study have considerable merit, as they not only help to understand the relative importance of parameters and processes in a qualitative manner, but also allow for a much better performance with respect to computer time and data handling than a fully three-dimensional study.

### 6.1 Heating Schedule

Several considerations guide the choice of a desirable heating schedule for the DST. The basic consideration is based on one of the thermal goals of the repository design, namely that the drift wall temperature should not exceed 200 °C. This constraint limits the maximum heat input into the test. On the other hand, the objective of the DST to monitor the coupled thermal, mechanical, chemical, and hydrological processes in the compressed time frame of a field test (years rather than hundreds of years in a real repository) involves the necessity of injecting in a maximum load of heat into the rock mass in a short time. Another consideration is that certain experiments, particularly the hydrochemical tests, need to be conducted in a quasi-steady environment. Thus the near-heater temperatures should remain relatively unchanged for several

almost identical. This is not a surprise considering that the total heat input into the DST during the 4 years of heating differs only as much as 2% between the two cases.

Table 6.1-1: Maximum drift wall temperature and dry-out rock volume for different heating schemes (C = crown; B = bottom; S = springline; BC = Base Case)

Scenario No	Time Period	Heater Power (%)		Temp. at 2 yrs (°C)			Temp. at 4 yrs (°C)			dry-out rock volume (m <sup>3</sup> /m x 1000)	
		in-drift	wing	C	B	S	C	B	S	2 yrs	4 yrs
1	4 years	80	80	176	191	213	254	266	293	188.4	407.9
2	1 year	80	0	145	160	178	233	245	272	102.3	347.9
	3 years	80	80								
3	1 ½ years	80	80	144	157	179	198	209	237	179.0	381.2
	2 ½ years	50	80								
4	1 ½ years	80	80	141	154	170	176	184	201	163.0	288.0
	2 ½ years	50	50								
BC	1 year <sup>*1</sup>	100	100	145	158	172	175	184	200	169.3	290.9
	3 years	50	50								
BC	1 year <sup>*2</sup>	100	100	144	153	169	172	179	196	171.0	272.7
	3 years	50	50								

\*1 2-D simulation results for base-case heater schedule as introduced in Section 5 of this report.

\*2 3-D simulation results for base-case heater schedule as introduced in Section 5 of this report.

## 6.2 Dual Permeability

In this section, a dual permeability formulation is applied for modeling the thermal-hydrological behavior of the rock mass, as opposed to the ECM model previously used. A dual permeability model is able to capture the transient response in the matrix to perturbations of temperature, pressure, or saturation in the fractures. In other words, fracture and matrix continua do not need to be in thermodynamic equilibrium at all times, as assumed with the ECM. The matrix is represented by *one* continuum, i.e., a *dual* permeability formulation rather than a “MINC” (Multiple Interacting Continua, after Pruess and Narasimhan, 1985) formulation is applied. This means that the fracture-matrix interaction is proportional to the primary variable difference between the

More prominent differences between DKM and ECM are evident in the vertical saturation profiles shown in Figures 6.2-4 and 6.2-5. While the vertical extent of the dry-out rock volume above and below the Heater Drift is almost identical, and while the build-up of saturation in the condensation zone immediately adjacent to the dry-out zone is similar for the two cases, the saturation profiles show a clearly different behavior further away from the heated area. In the DKM, the saturation perturbation in the fractures migrates much further than in the matrix. This is particularly evident in the vertical downward direction, indicating that there is a large region of enhanced gravity-driven flux. In fact, the perturbation of saturation in the fracture continuum extends all the way to the bottom of the model area. As this jeopardizes the validity of the initially chosen constant-pressure boundary condition, a "free drainage" boundary condition was applied instead (McCord, 1991). In contrast, the ECM model gives a much less extended region of fracture saturation build-up above and below the heater. The reason for this behavior is in the different dynamics of the thermal-hydrological response in fractures and matrix, which cannot be captured with the equilibrium assumption associated with ECM. As vapor is driven away from the heaters, it will eventually condense at the fracture walls, and liquid saturation in the fractures will increase. This gives rise to significantly enhanced liquid flux in the fractures, away from the condensation zone. At the same time, part of the liquid imbibes into the matrix, as a capillary pressure gradient between the fractures and the matrix develops. However, as matrix imbibition is relatively slow, some fraction of the condensate can migrate very far in the fractures before being affected by that process. The ECM concept cannot capture this retarded response in the matrix; it assumes a pressure equilibrium between fractures and matrix at all times, which essentially means that the imbibition rate is strong enough to guarantee a zero response time. Therefore, the ECM results underestimate the potential for gravity-driven liquid flux far away from the near-heat environment.

Another interesting aspect can be seen in Figure 6.2-2, which presents the evolution of the dry-out rock volume estimated from the two models. Almost identical during the heating period, the curves show significant differences during cooling. For the DKM, the rewetting is much slower; in fact, the dry-out rock volume even increases for another year after the heaters are turned off before eventually starting to show some effect of moisture reflux into the dry-out zone. Our interpretation is that these differences are less a result of the DKM having a better capability of modeling the dynamics of this cooling process, and more a result of the fact that during heating, the DKM yields higher liquid flux away from the condensation zone in the vertical downward direction, leaving less liquid available to be drawn back toward the heat source when the heaters are turned off.

Our results indicate the importance of the model conceptualization. However, both ECM and DKM give similar results for the near-heater environment, in particular the rock volume bracketed by the hydrology holes. Therefore, the predicted readings of temperature, gas pressure, and saturation in the hydrology holes are not expected to be affected by the model formula-

## 7 Prediction of Sensor Reading in Hydrology Holes

The model results from the three-dimensional thermal-hydrological simulations presented in Section 5 above are used here to predict readings of temperature, gas pressure, and relative humidity in the 12 hydrology holes during the heating and cooling phases of the test. In addition to the passive monitoring, single-hole and interference air injection tests will be performed in isolated sections of the hydrology holes. Therefore, the effect of moisture redistribution on air permeability tests is also discussed in this section. However, no explicit simulation of air injection tests has been performed in this study, since the test configuration with the specific packer and sensor location in each hydrology hole has yet to be finalized. In fact, the model predictions will provide guidance as to which zones should be used for air injection, where along the boreholes packers and sensors should be placed, and at what specific time intervals injection tests should be performed. However, the reader should keep in mind that the simulation runs are done without taking local heterogeneities into account. It is thus to be expected that the actual measurements will deviate from the predictions. The heterogeneity information will be forthcoming, as pre-heat air permeability tests will be conducted for the hydrology holes.

The predicted sensor readings in all 12 hydrology holes are shown in Appendix A1 for the 3.6 mm/yr infiltration scenario, and in Appendix A2 for the 0.36 mm/yr infiltration scenario. In both cases, the heat transfer from canisters to the drift wall is represented by the uniform heat load boundary conditions, assuming little radiative heat exchange within the drift. The heaters are operating at full power for 1 year, followed by 3 years heating with 50% power before heat is finally turned off and a passive cooling period begins. The thermal-hydrological conditions seen at certain locations in the boreholes are interpolated from the nearest grid points of the 3-D model, since the borehole geometry, packer and sensor locations are not explicitly represented in the grid design. In doing so, the interpolated thermal-hydrological state represents a very local situation in the borehole, while in reality the sensor readings will always represent a longer section along the borehole, namely the length of the packed-off zones. Thus, our predictions of sensor readings can only be an *estimate* of the real system response.

The first sections of Appendices A1 and A2 show the temperature evolution during 4 years of heating and 4 years of cooling at 36 representative sensor locations in the hydrology holes. In each hole, three hypothetical sensors are placed at distances of 9.5 m, 19.5 m and 29.5 m from the collar in the Observation Drift, measured in the horizontal direction and referred to in the figures as borehole number plus subscript 2, 4 and 6, respectively. For example, the notation 59<sub>6</sub> refers to a sensor in borehole 59 placed at a horizontal distance of 29.5 m from the collar. Predictions have been made for a total number of 8 hypothetical observation points in each hole, but only three of these are shown in the figures, therefore the indices 2, 4, and 6. The chosen

tures along a significant portion of the borehole have already exceeded the nominal boiling point, and the matrix saturations have started to decrease significantly (i.e., the boreholes intersect the dry-out zone that develops around the heaters). The maximum temperatures will be seen in hydrology hole 77, as high as 145 °C for 3.6 mm/yr infiltration and 155 °C for 3.6 mm/yr infiltration. A significant gas pressure build-up will be observed as soon as the temperatures approach the nominal boiling point. After the heat is turned off, the matrix saturations remain very low during the entire monitoring period, since the rewetting process is very slow.

- Boreholes 59, 61, 76, 78 and 186 fall into the second category which might be characterized as “hot and wet.” Soon after heating begins, the matrix saturations increase due to the condensation of vapor. The temperatures rise quite fast to about 100 °C typically after 1 year of heating, but thereafter remain at this temperature state for a long time period. In fact, for 3.6 mm/yr infiltration, the temperatures stay constant around 100 °C throughout the entire remaining heating period. At the same time, the matrix saturations may slowly decrease, but essentially remain in a “wet” state, as the temperatures apparently do not significantly exceed the nominal boiling point. Only hydrology holes 76 and 78 will see a substantial reduction of the matrix saturation, but only in the final period of heating after 4 years. It seems that at this time the thermal-hydrological situation along boreholes 76 and 78 is changing from a “hot and wet” to “hot and dry” condition. The results for 0.36 mm/yr infiltration show a similar, but more distinct behavior in that the initial saturation build-up in the matrix is more pronounced, and that the above-described transition from one thermal-hydrological state to the other takes place slightly earlier. In order to fully capture this transition, the heater test should be operated with a heating period of no less than 4 years, ideally even longer than that. Gas pressures will noticeably build up throughout the heating period; however, the pressure response will be slower and less pronounced than for the “hot and dry” boreholes.
- The last category comprises the boreholes furthest away from the heaters, namely hydrology holes 57, 58, 74, 75 and 185. The temperature along these boreholes will stay below the nominal boiling point at all times. The matrix saturations increase due to condensation of vapor and stay above the initial saturation during the entire heating period. After heat is turned off and the rock mass starts cooling down, the high saturation values slowly return to pre-heat conditions, as water is driven by strong capillary forces to the dry-out zones. Note that all boreholes in this category are located above the Heater Drift and intersect the interface between the tptpmn and the tptpul unit, as evident from the drop in the saturation profiles. The pressure sensors are not expected to register readings much different from the ambient value during passive monitoring; only boreholes 58 and 75 may see a slight gas pressure build-up at 4 years of heating.

sure response is far too complex to be analyzed or predicted in this design study.) The following results can be expected from single-hole air permeability tests:

- The hydrology holes categorized as “hot and wet” or “warm and wet” are expected to show an increased single-hole pressure response to air injection, as the gas-phase permeability in the surrounding rock decreases with time after heat is turned on. All these boreholes are partially located in the condensation zone, where matrix and fracture saturations build up due to condensation of vapor. Supposing that the packed-off injection zone is appropriately placed along the boreholes, injection tests will be able to detect this build-up. Once the saturation has increased, the hydrology holes further away from the heater, namely 57, 58, 74, 75, and 185, remain at this “wet” state throughout the heating and some part of the cooling period; i.e., they will probably show a similarly high pressure response throughout most of the testing. Other hydrology holes closer to the wing heaters or the Heater Drift, namely 59, 61, 76, 78, and 186, are expected to show a similar build-up of injection pressure throughout the first few years of heating, but a reversed situation at the end of the heating period, as the local liquid saturation slowly decreases to or even below the pre-heat values.
- Sensors placed in hydrology holes categorized as “hot and dry” will reveal a significant decrease of liquid saturation along the near-heater borehole sections soon after heating starts. As pointed out before, this decrease can be detected with the relative humidity readings. However, it is very unlikely that these saturation changes will be detectable in air injection tests, as the fractures start with low saturation values at ambient state, and the minor saturation decrease due to the dry-out will not noticeably change the gas relative permeability.
- The simulation results presented in Section 5 reveal an extended zone of increased saturation below the heated areas, indicating that relatively fast gravity-driven flux is expected to occur in the fractures. According to the ECM simulation runs, this zone may extend as much as 50 m in the vertical downward direction after 4 years of heating; according to the DKM runs, it may be even larger. However, with the present configuration of hydrology holes, there is no direct way of detecting potentially enhanced liquid flux in the fractures far below the heater area. Hydrology holes 61, 78 and 186, which bracket the heater area from the lower end, are only covering part of the condensation zone, with z-coordinates of about -12.5 m at the bottom of the boreholes. This limitation in test configuration is particularly unfortunate since the two fracture-matrix interaction models applied in this study, ECM and DKM, show considerable differences with respect to gravity-driven liquid flux, but there will be no potential for directly detecting the real system behavior and thereby evaluating the validity of these concepts.

## 8 Summary

We have presented the results of the modeling of both the heating and cooling phases of the Drift Scale Test. The impact on the thermal-hydrological conditions in the rock mass from different input parameters such as heating rates and schedules, different percolation fluxes at the test horizon, and alternative conceptualization of the matrix-fracture interaction such as the effective continuum model and the dual permeability formulation were discussed. In particular, the simulations give the expected readings on the humidity, temperature and pressure sensors due to their response to the changing thermal-hydrological conditions in the Drift Scale Test (DST). Furthermore, with regard to the active air permeability tests to be conducted in the hydrology holes during the DST, we discussed when, where, and how the pressure response will occur. These simulated results provide guidance to the location of the high-temperature packers and sensors yet to be installed in the hydrology holes.

The results presented indicate that the optimum heating scheme would be to apply almost full heater power at the beginning of the test to enforce a fast response in the DST, followed by a long period of reduced power output during which the temperatures are maintained at the desired level. The results also confirmed that the DST should be a long-term test, that a heating period of at least 4 years is desired, in order (1) to have the benefit of collecting more complete data on the wetting and drying phenomenon monitored by the sensors in the hydrology holes, (2) to be able to maintain quasi-steady thermal-hydrological conditions for a sufficiently long time period which is a favorable environment for certain experiments planned in the DST.

The conclusions of this report are mainly based on qualified data and qualified software. The simulations presented were performed with a numerical model employing what we considered to be the "best" input parameters and "most reasonable" conceptualization. The properties were based on (1) the UZ site-scale model calibration of a surface-to-water-table column at well SD-9, and (2) laboratory and field measurements at the DST area. A complex 3-D grid design was developed to resemble the DST configuration as closely as possible. Where uncertainty due to parameter and conceptualization was anticipated, special care was taken to discuss their impact on the simulated results. Therefore, the presented model provides insight into how the DST is expected to perform and how to conduct the DST. It will serve as a baseline model upon which as-built data, further characterization data, and actual monitoring data may be used for refining and calibrating.

- Doughty, C. and G.S. Bodvarsson, 1997. Investigation of conceptual and numerical approaches for evaluating moisture flow and chemical transport, Chapter 5 of The site-scale unsaturated zone model of Yucca Mountain, Nevada, for the Viability Assessment, G.S. Bodvarsson, T.M. Bandurraga, and Y.-S. Wu, eds., Yucca Mountain Project Milestone Report SP24UFM4, DTN: LB9706001233129.001, Lawrence Berkeley National Laboratory Report, Berkeley, CA.
- Edlefsen, N.E. and A.B.C. Anderson, 1943. Thermodynamics of soil moisture, ACCN: NNA.19900312.0151, Hilgardia, vol. 15, no. 2, pp. 31-298.
- Finsterle, S., 1993. ITOUGH2 user's guide, version 2.2, Lawrence Berkeley National Laboratory Report LBNL-34581, UC-600, ACCN: MOL.19941026.0075, Lawrence Berkeley National Laboratory, Berkeley, CA.
- Finsterle, S., K. Pruess, and P. Fraser, 1996. ITOUGH2 software qualification, Lawrence Berkeley National Laboratory Report LBNL-39489, UC-800, ACCN: MOY-970206-04, Lawrence Berkeley National Laboratory, Berkeley, CA.
- Flint, A.L., J.A. Hevesi, and L.E. Flint, (in preparation). Conceptual and numerical model of infiltration for the Yucca Mountain area, Nevada, U.S. Geological Survey Water-Resources Investigation Report, ACCN: MOL.19970409.0087, DTN: GS960908312211.003, U.S. Geological Survey, Denver, CO.
- Flint, L.E., (in preparation). Matrix properties of hydrogeologic units at Yucca Mountain, Nevada, U.S. Geological Survey Open-File Report, ACCN: MOL.19970324.0046, DTN: GS950308312231.002 (Q), U.S. Geological Survey, Denver, CO.
- Freifeld, B. and Y. Tsang, January 1997a. Letter report on first quarter results of measurements in hydrology holes in single heater test area in the ESF, Yucca Mountain Project Milestone Report SP9263M4, ACCN: MOY-970513-01, DTN: LB970100123142.001, Lawrence Berkeley National Laboratory, Berkeley, CA.
- Freifeld, B. and Y. Tsang, May 1997b. Letter report on second quarter results of measurements in hydrology holes in single heater test area in the ESF, Yucca Mountain Project Milestone Report SP9216M4, DTN: B970500123142.001, Lawrence Berkeley National Laboratory, Berkeley, CA.
- Hinds, J., T.M. Bandurraga, M.A. Feighner, and Y.S. Wu, 1997. Geology of the unsaturated zone and the UZ model, Chapter 3 of The site-scale unsaturated zone model of Yucca Mountain, Nevada, for the Viability Assessment, G.S. Bodvarsson, T.M. Bandurraga, and Y.-S. Wu, eds., Yucca Mountain Project Milestone Report SP24UFM4, DTN: LB9706001233129.001, Lawrence Berkeley National Laboratory Report, Berkeley, CA.
- Ho, C.L. and S.W. Webb, 1996. A review of porous media enhanced vapor-phases diffusion mechanisms, models and data-does enhanced vapor-phase diffusion exist?, Technical Report, SAND96-1198, Sandia National Laboratories, Albuquerque, NM.

- Vargaftik, N.B., 1975. *Tables of the Thermophysical Properties of Liquids and Gases in Normal and Dissociated States*, John Wiley & Sons, Inc., ACCN: NNA.19940428.0016, 2nd Edition.
- Walker, W.R., J.D. Sabey, and D.R. Hampton, 1981. *Studies of heat transfer and water migration in soils*, Final Report, Department of Agricultural and Chemical Engineering, Colorado University, Fort Collins, CO.
- Wang, J. and R. Suárez-Rivera, 1997. *Laboratory test results of hydrological properties from dry drilled and wet drilled cores in the drift scale test area and in the single heater test area of the thermal test facility*, Yucca Mountain Project Milestone Report SP5130M4, DTN: LB970500123142.003, Lawrence Berkeley National Laboratory, Berkeley, CA.
- Wu, Y.-S., C.F. Ahlers, P. Fraser, A. Simmons, and K. Pruess, October 1996. *Software qualification of selected TOUGH2 modules*, Lawrence Berkeley Laboratory Report LBL-39490, UC-800, ACCN: MOL.19970219.000-0105, Lawrence Berkeley National Laboratory, Berkeley, CA.

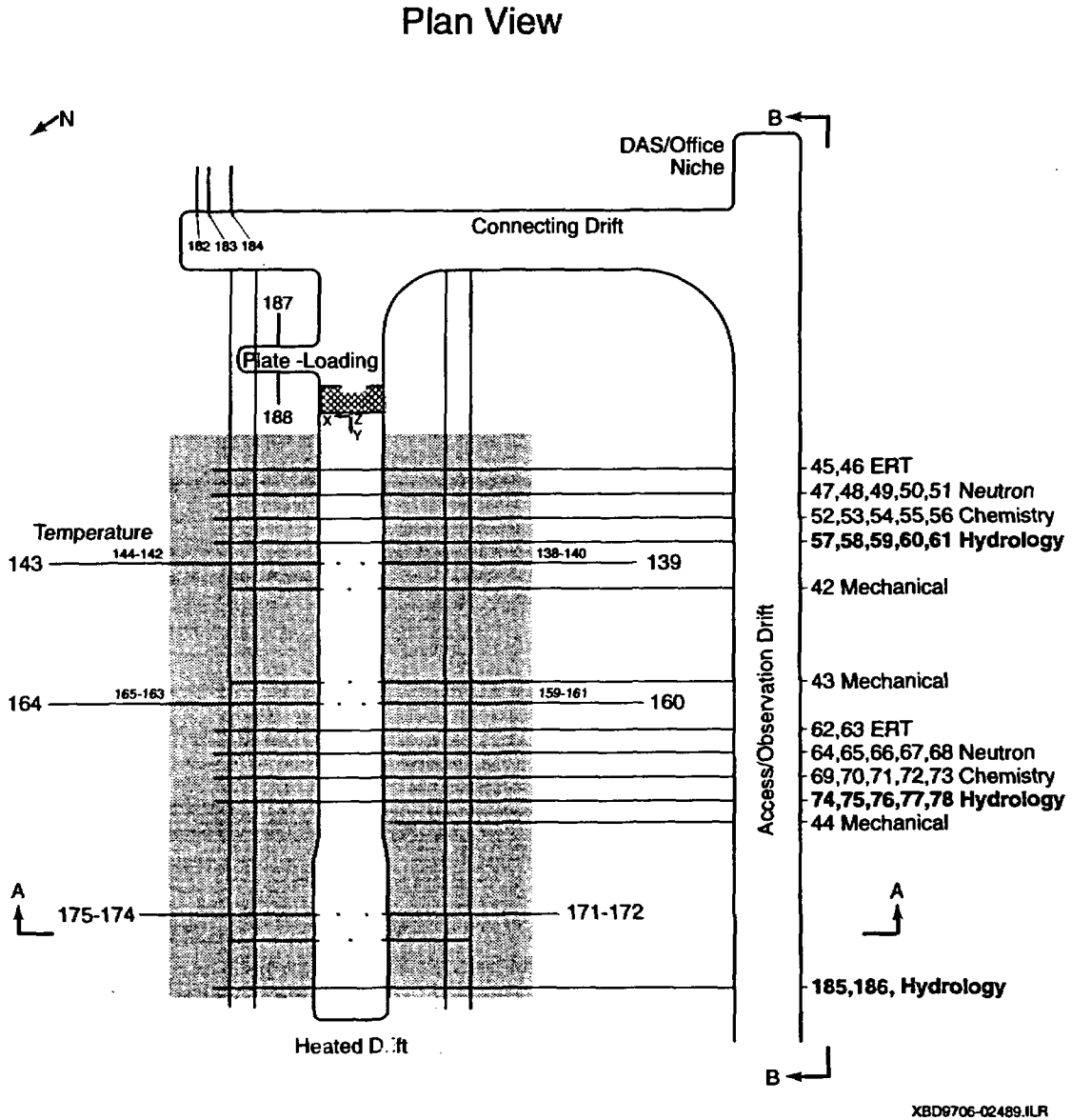
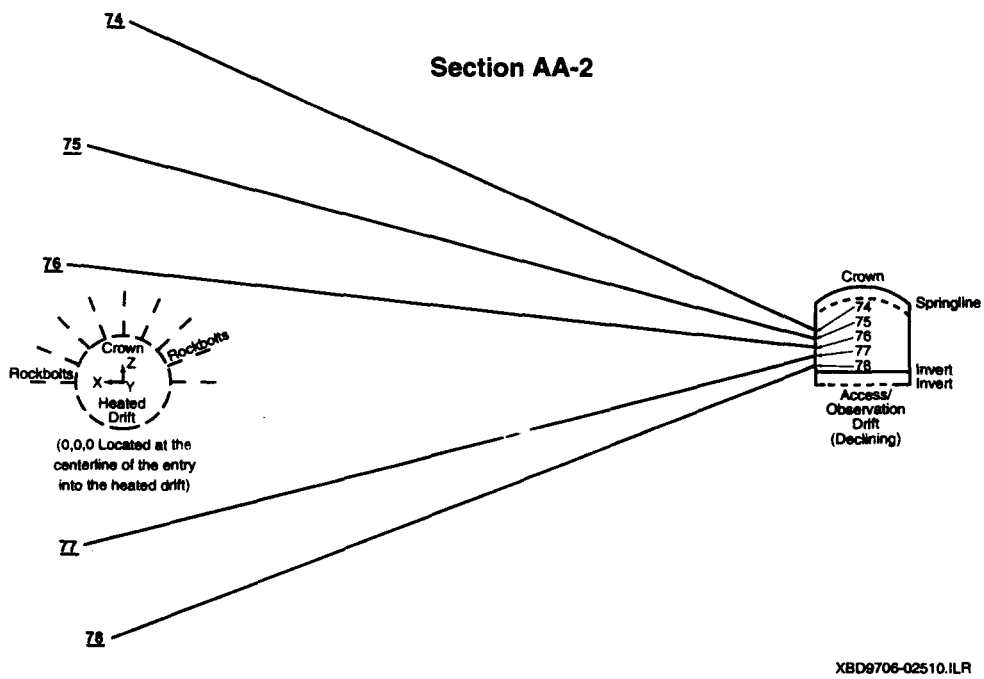
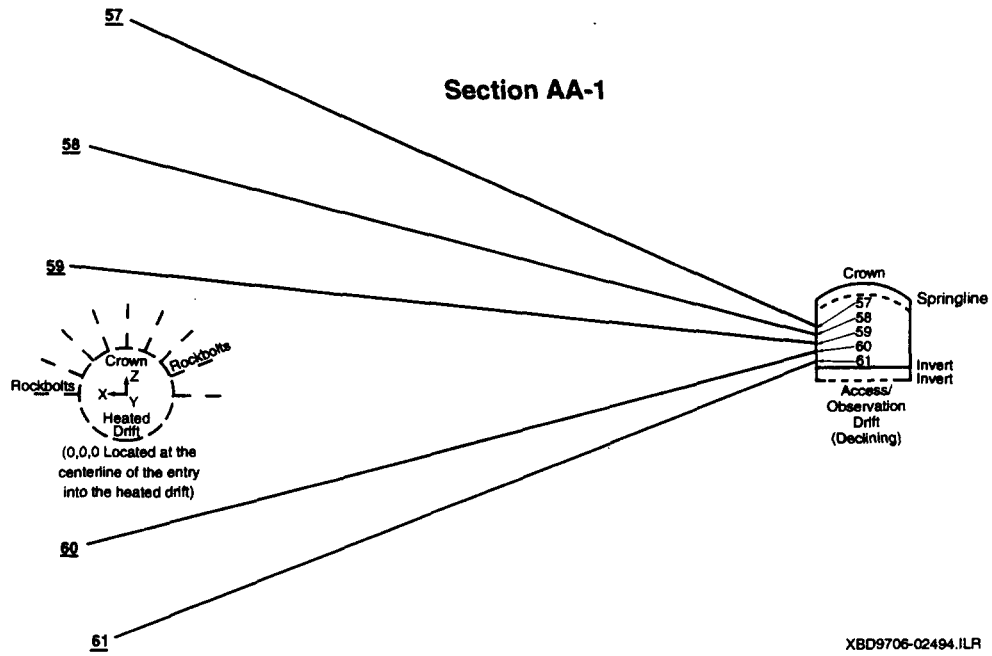


Figure 3.1-1 Plan view of the Drift Scale Test area. The shaded area represents the wing heaters.



**Figure 3.1-2** Vertical profile of the Drift Scale Test area along Section A-A, showing the configuration of hydrology holes 57 through 61 and 74 through 78.

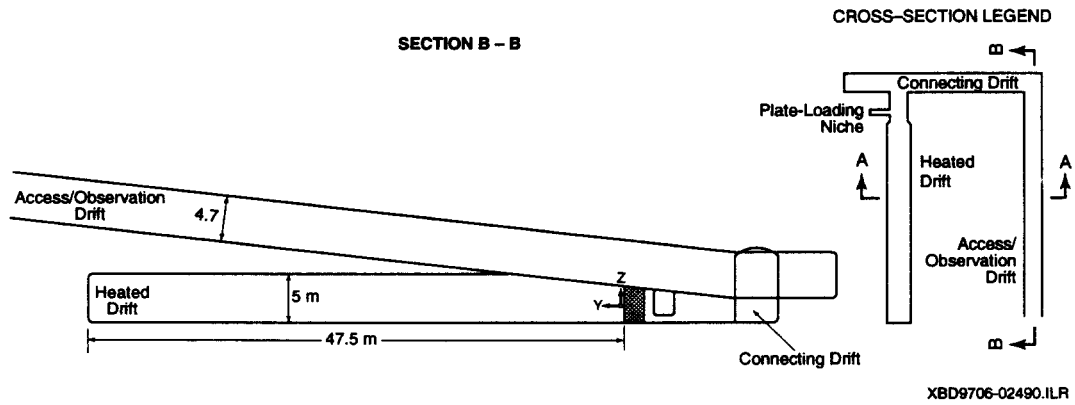


Figure 3.1-3 Vertical profile of Drift Scale Test area along Section B-B.

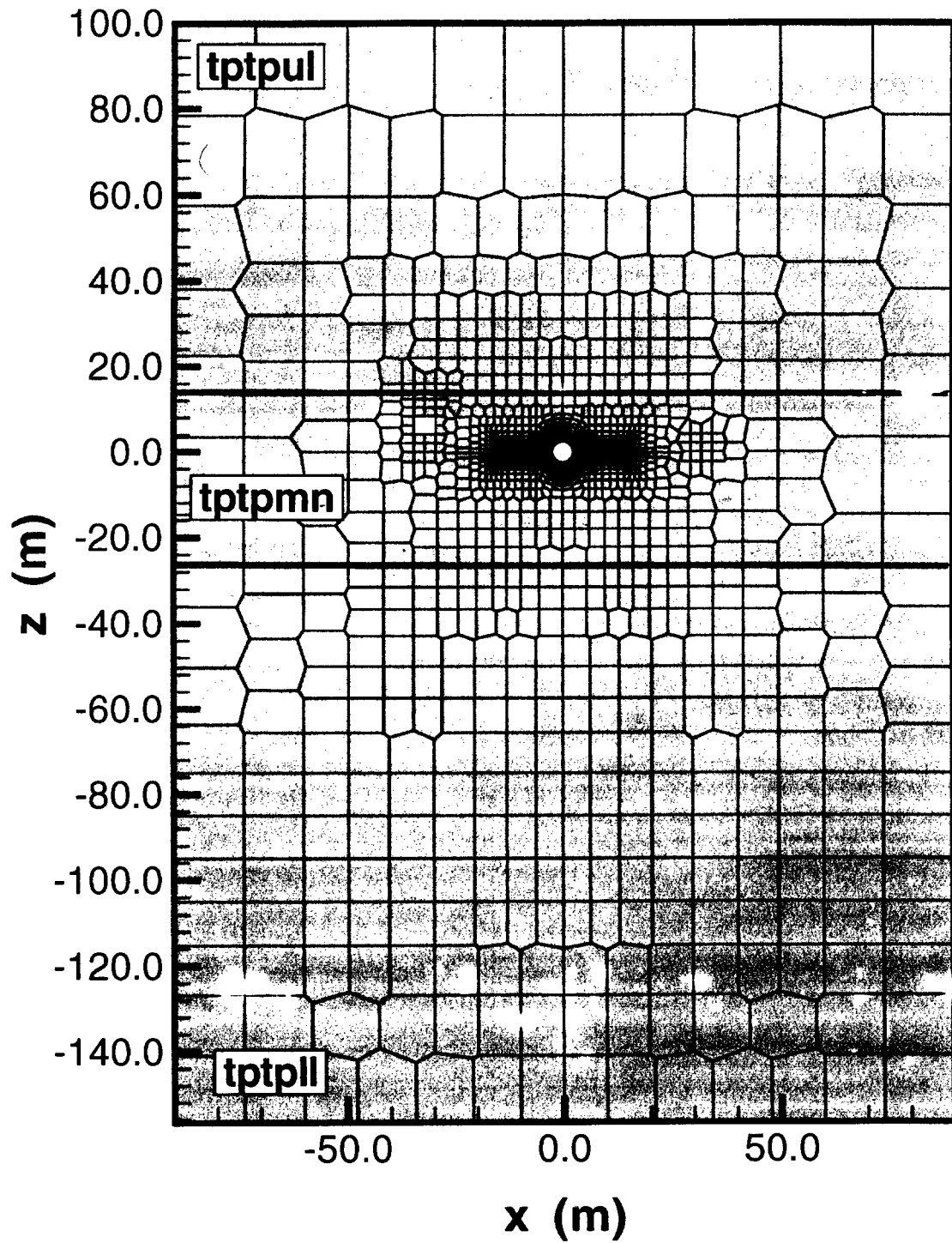


Figure 4.2-1 Discretization of the DST model in a typical xz-cross section.

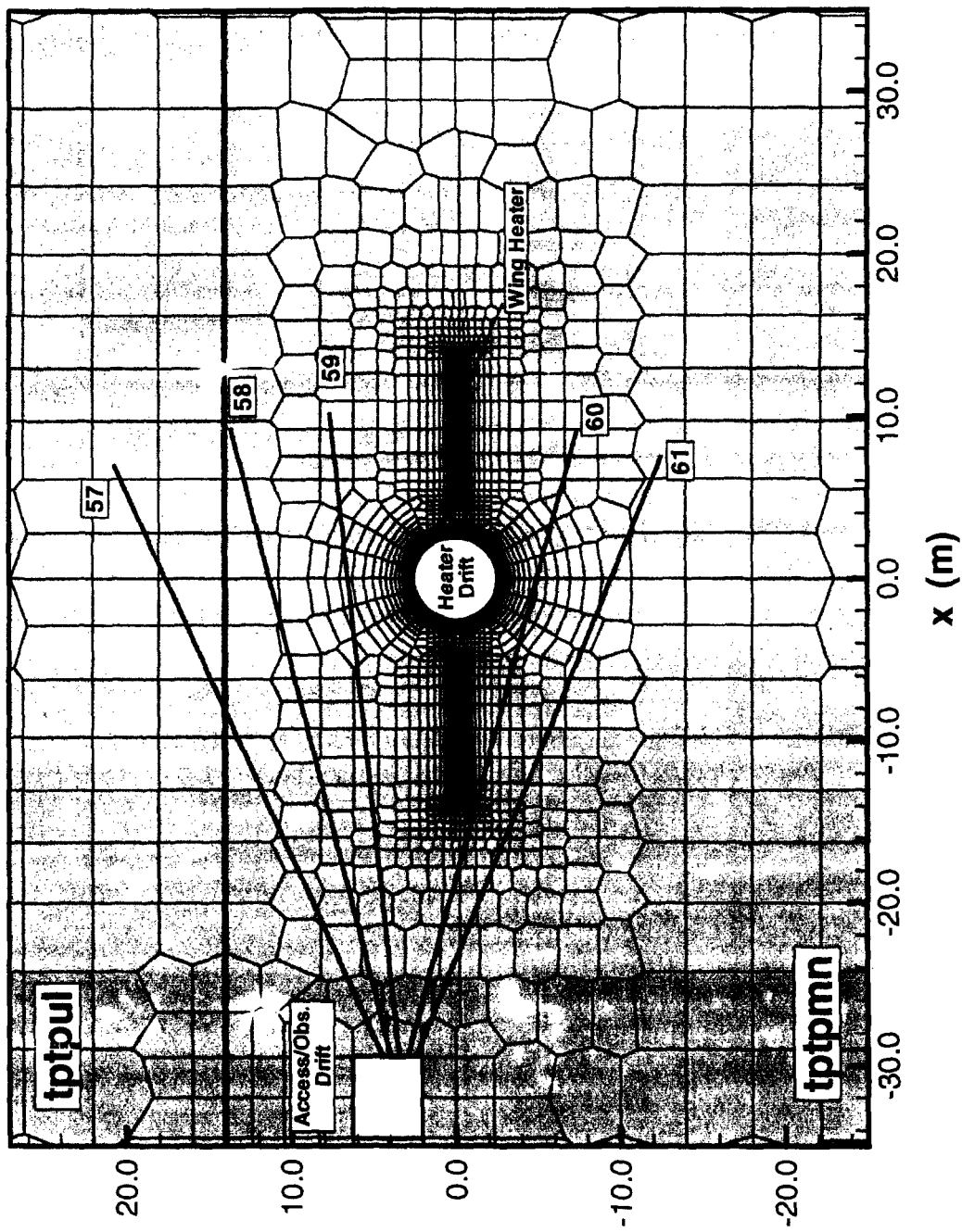


Figure 4.2-2 Discretization of the DST model in xz-cross section at  $y=10.06$  m, focusing on the near-drift area. Also presented is the location of hydrology holes 57 through 61.

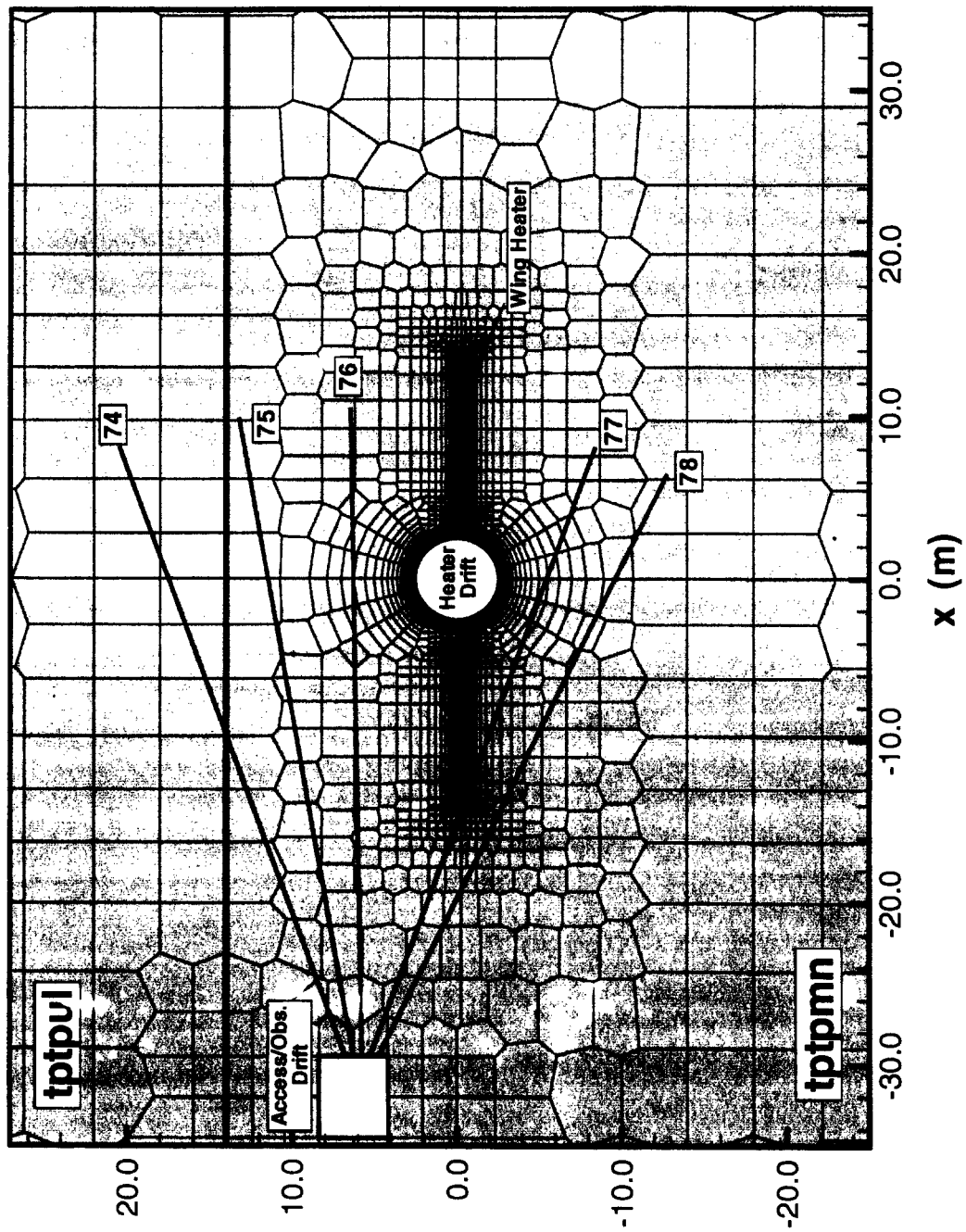


Figure 4.2-3 Discretization of the DST model shown in xz-cross section at  $y = 30.18$  m, focusing on the near-drift area. Also presented is the location of hydrology holes 74 through 77.

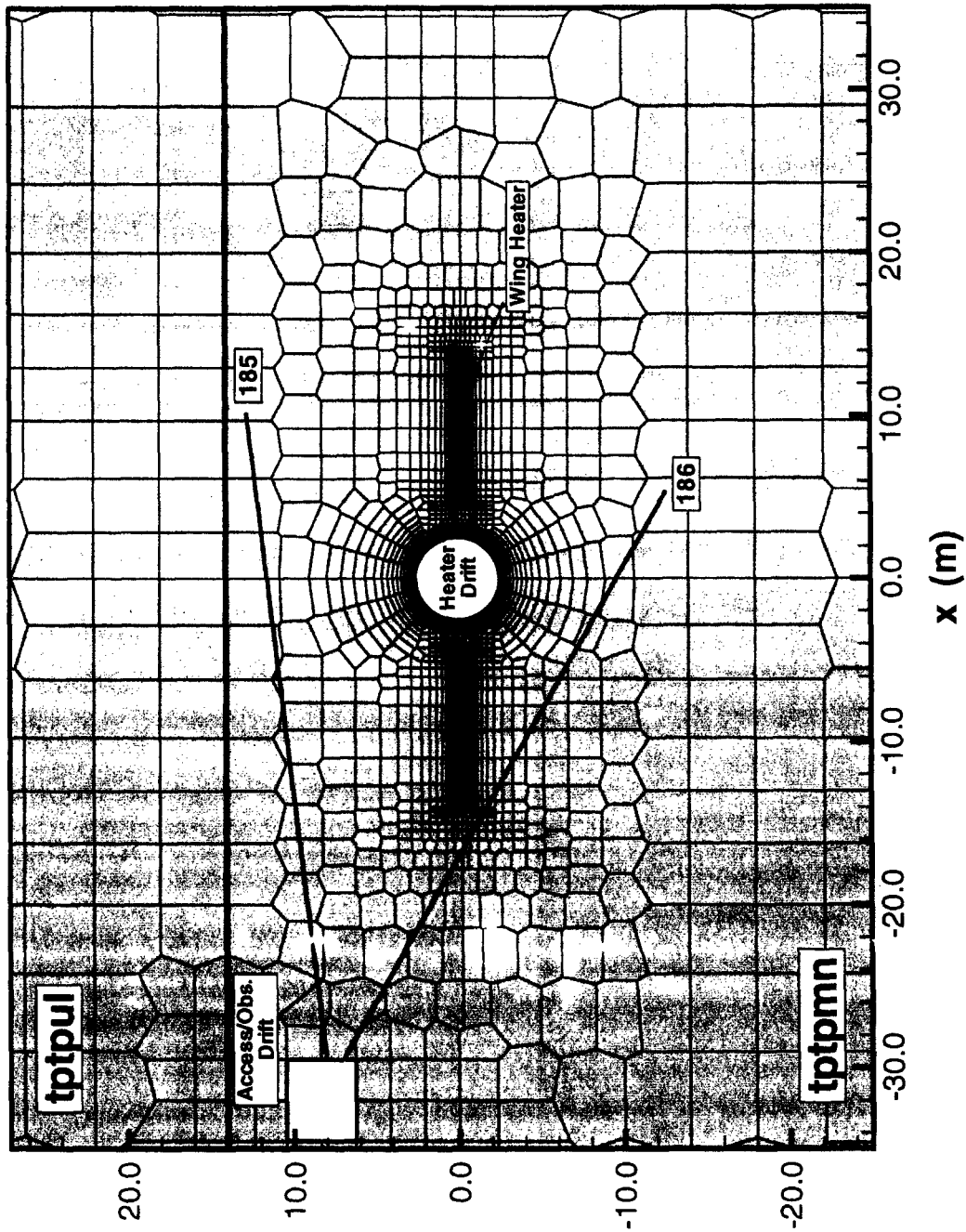


Figure 4.2-4 Discretization of the DST model shown in xz-cross section at  $y=44.8$  m, focusing on the near-drift area. Also presented is the location of hydrology holes 185 and 186

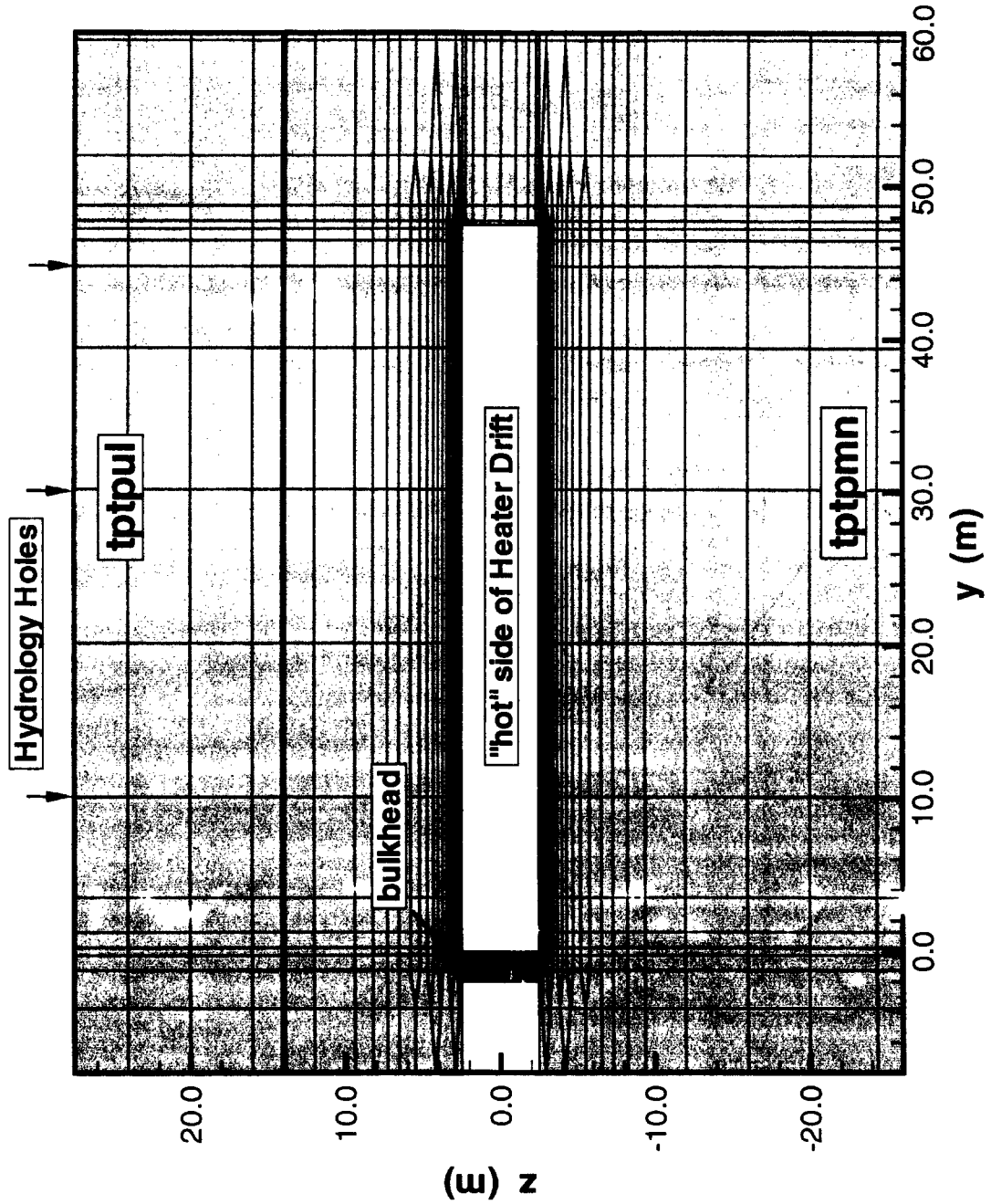


Figure 4.2-5 Discretization of the DST model shown in yz-cross section at  $x = 0.0$  m, focusing on the near-drift area. Also shown is the location of the three spatial clusters of hydrology holes.

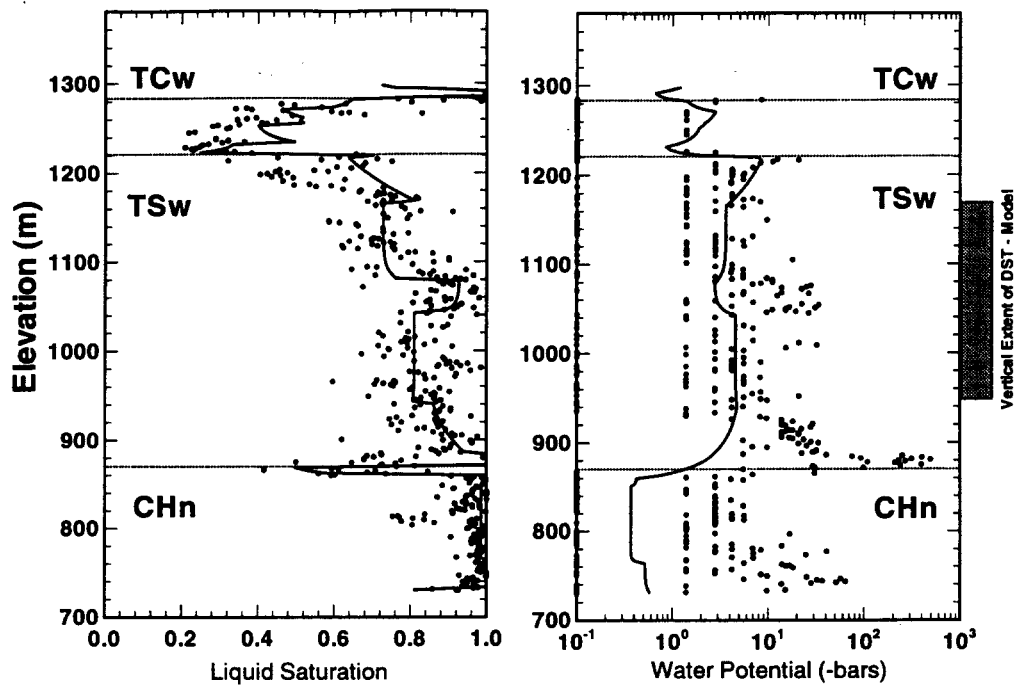


Figure 4.3-1 Calibrated saturation and water potential profiles from SD-9 inversion for 3.6 mm/yr infiltration case. Symbols indicate observed data.

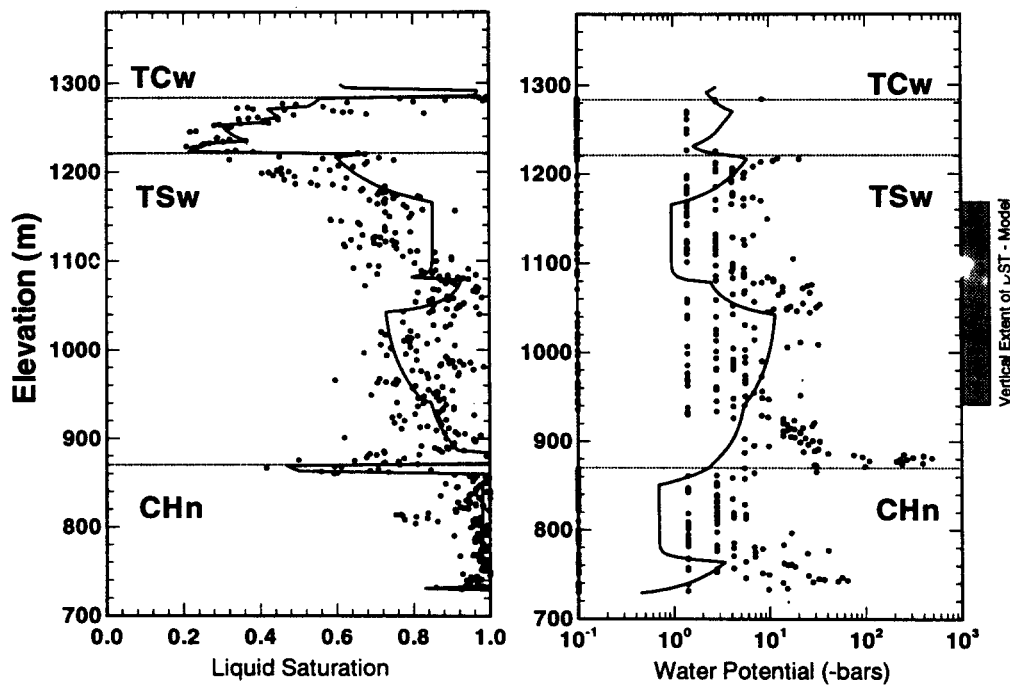


Figure 4.3-2 Calibrated saturation and water potential profiles from SD-9 inversion for 0.36 mm/yr infiltration case. Symbols indicate observed data.

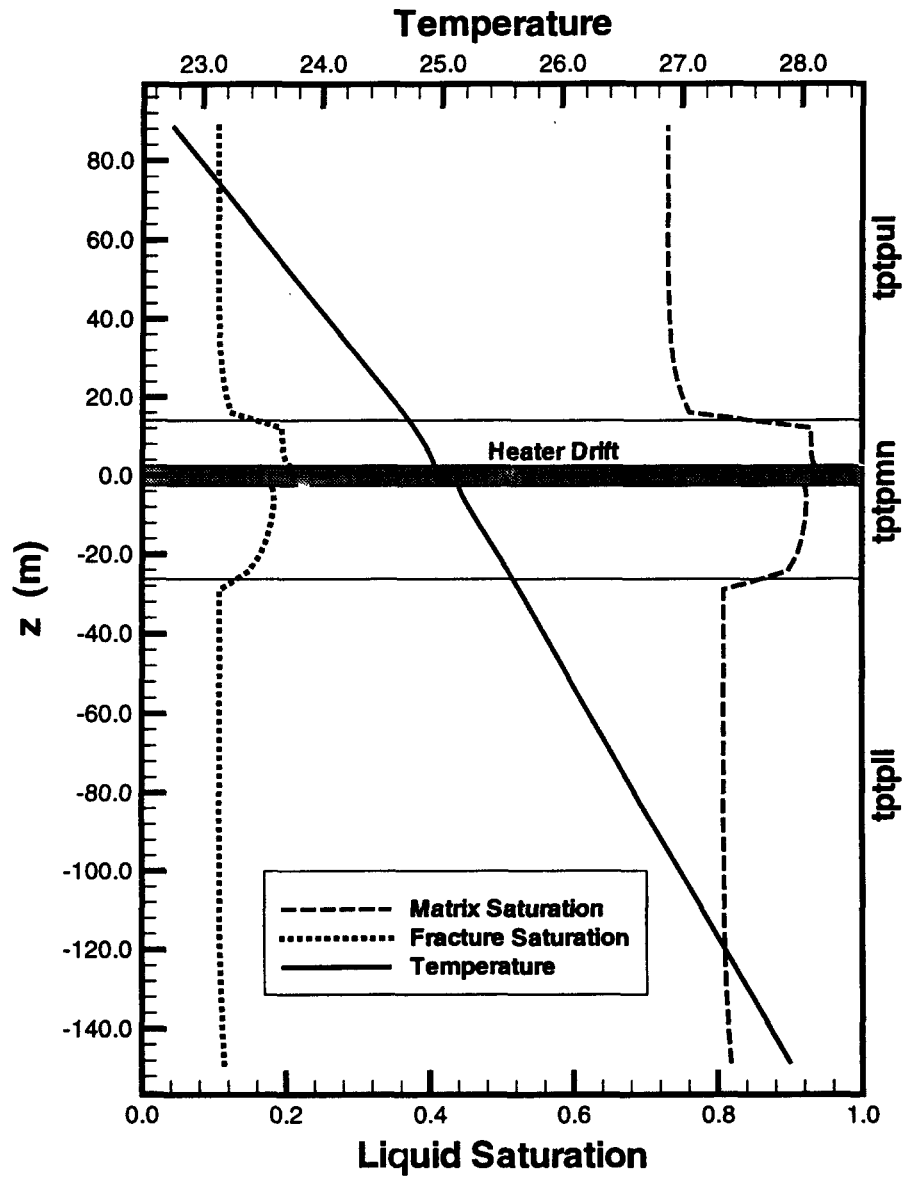


Figure 4.4-1 Initial saturation and temperature profile in DST model area measured along z-axis at  $x = 0.0$  m and  $y = 30.18$  m for 3.6 mm/yr infiltration case.

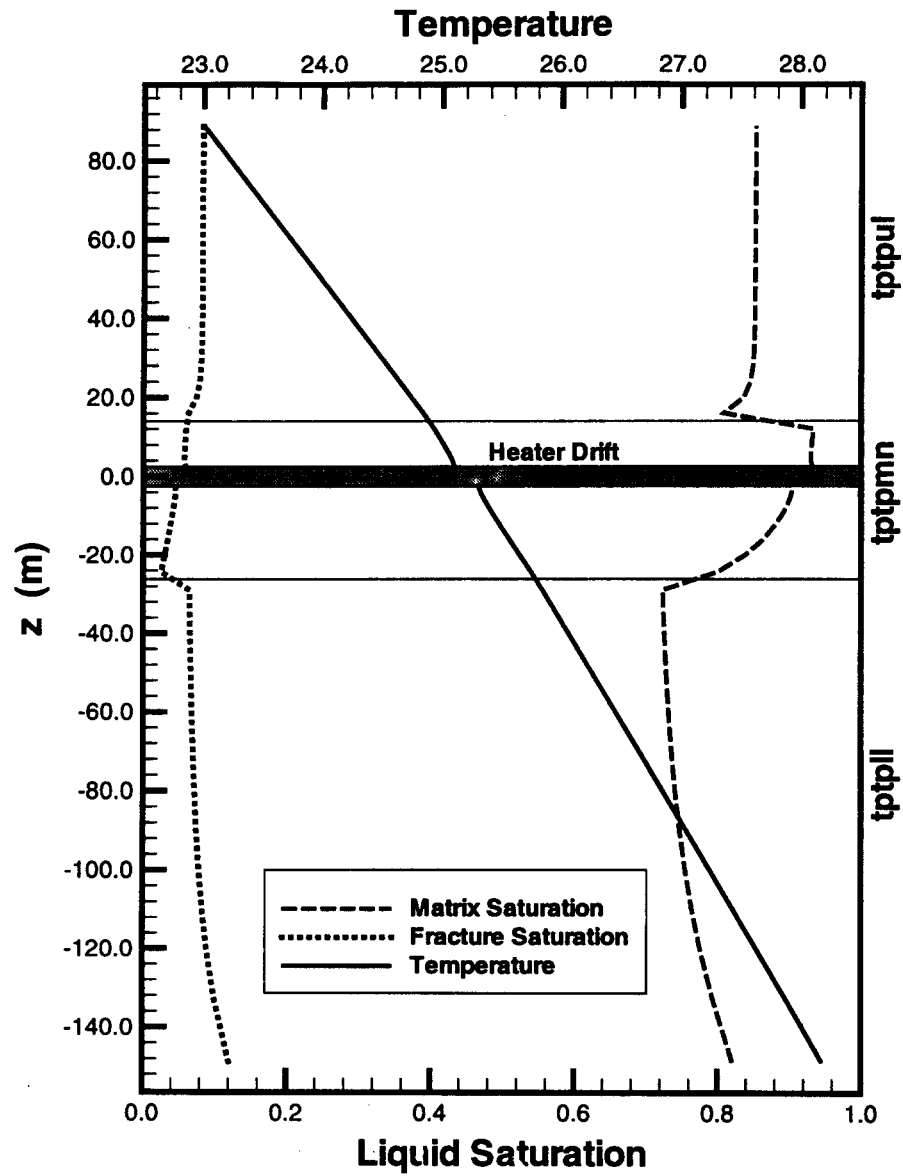


Figure 4.4-2 Initial saturation and temperature profile in DST model area measured along z-axis at  $x = 0.0$  m and  $y = 30.18$  m for 0.36 mm/yr infiltration case.

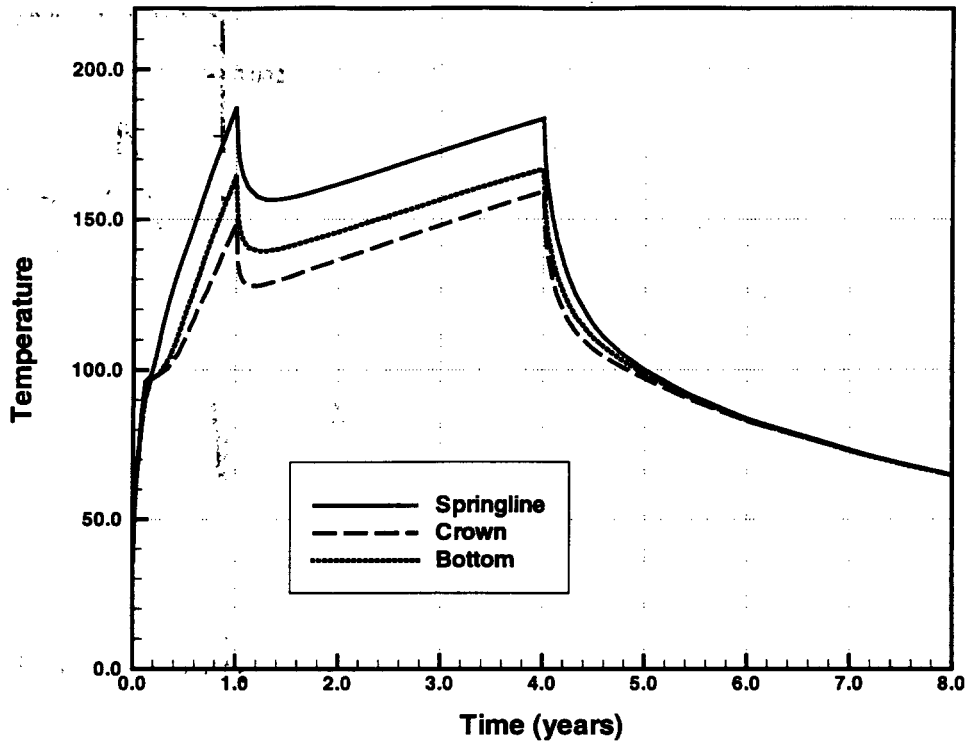


Figure 5.2-1 Temperature evolution at the heater drift wall at  $y = 10.06$  m from the bulkhead for 3.6 mm/yr infiltration case (1 year heating at 100%, 3 years heating at 50%).

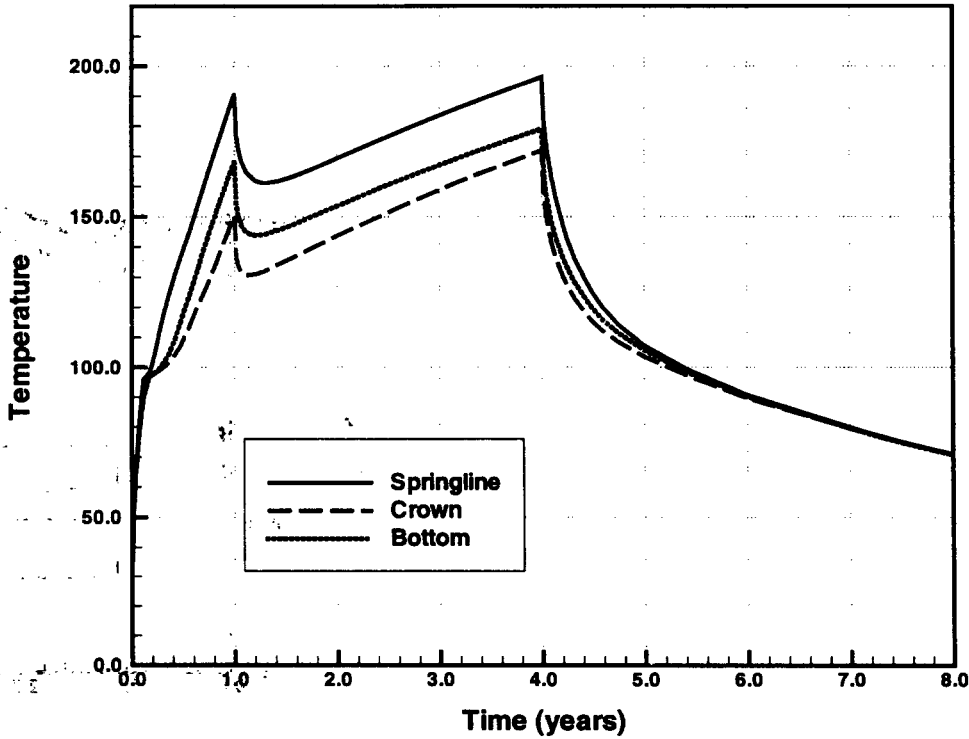


Figure 5.2-2 Temperature evolution at the heater drift wall at  $y = 30.18$  m from the bulkhead for 3.6 mm/yr infiltration case (1 year heating at 100%, 3 years heating at 50%).

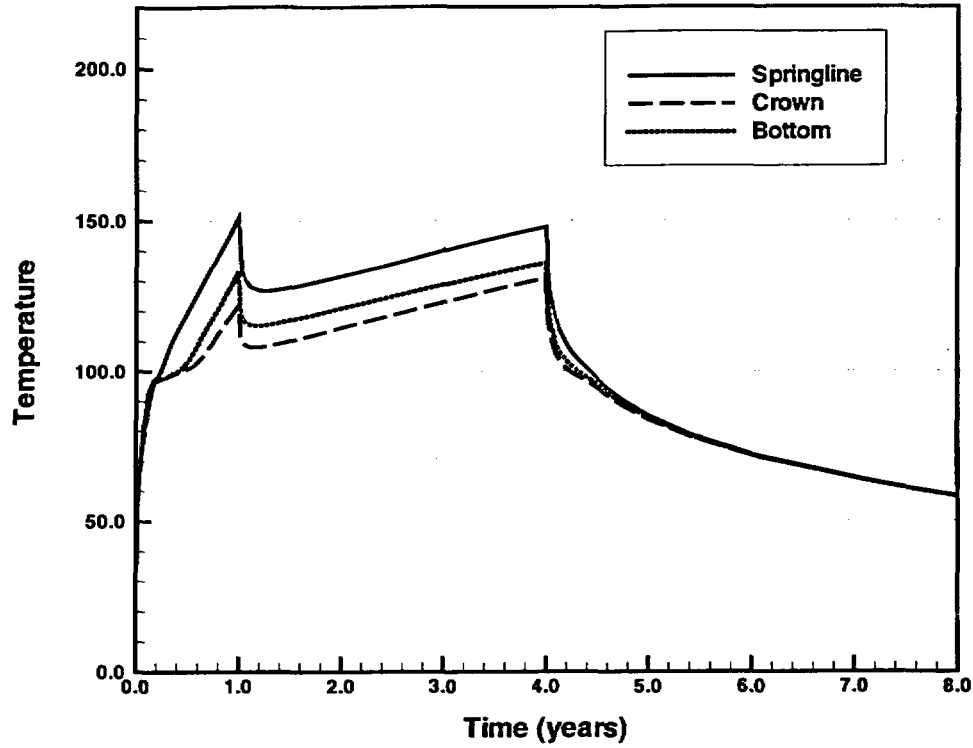


Figure 5.2-3 Temperature evolution at the heater drift wall at  $y = 44.8$  m from the bulkhead for 3.6 mm/yr infiltration case (1 year heating at 100%, 3 years heating at 50%).

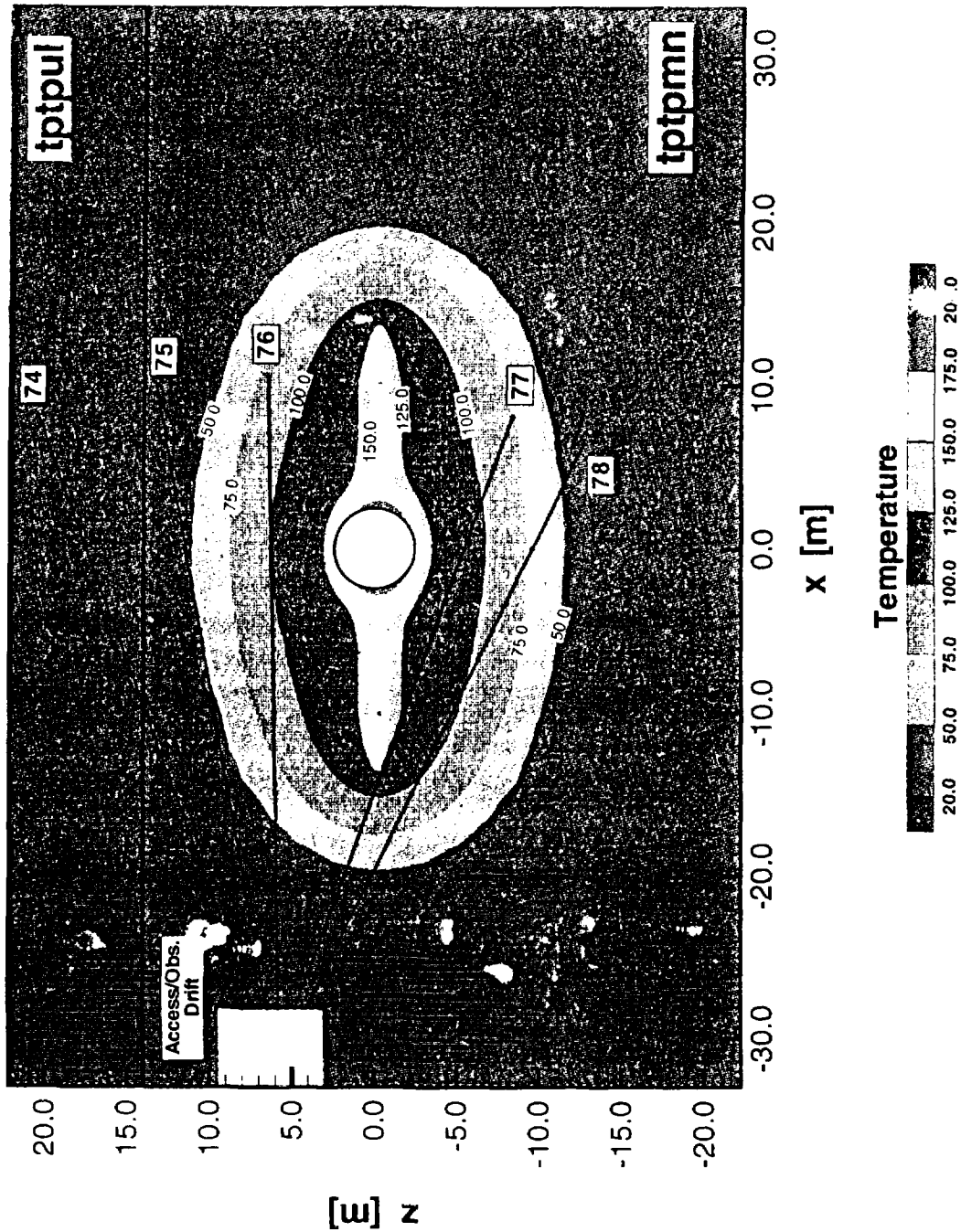


Figure 5.1-4 Temperature response after 1 year of heating in xz-cross section at  $y=30.18$  m for 3.6 mm/yr infiltration case (1 year heating at 100%, 3 years heating at 50%). Also presented is the location of hydrology holes 74 through 77.

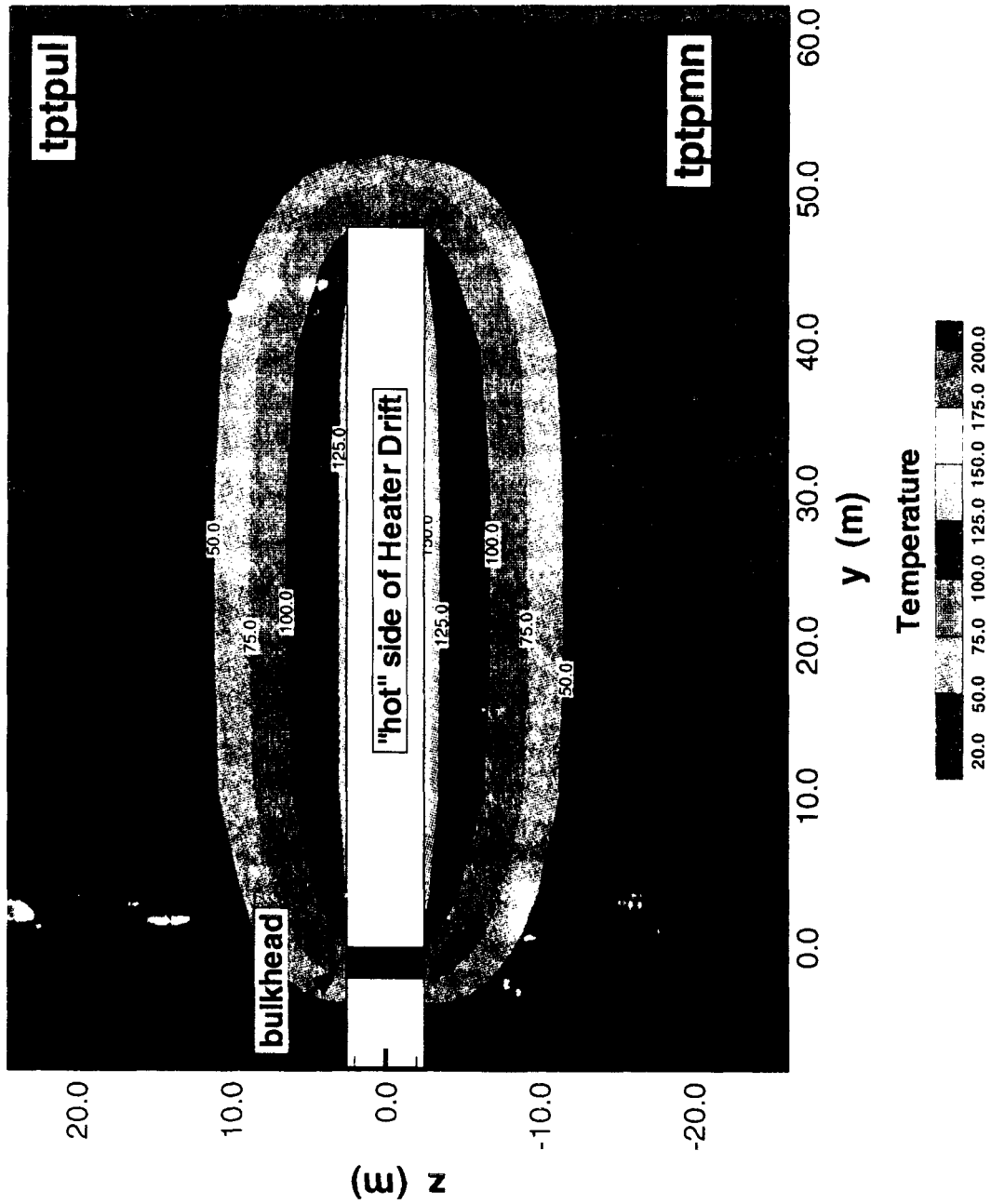
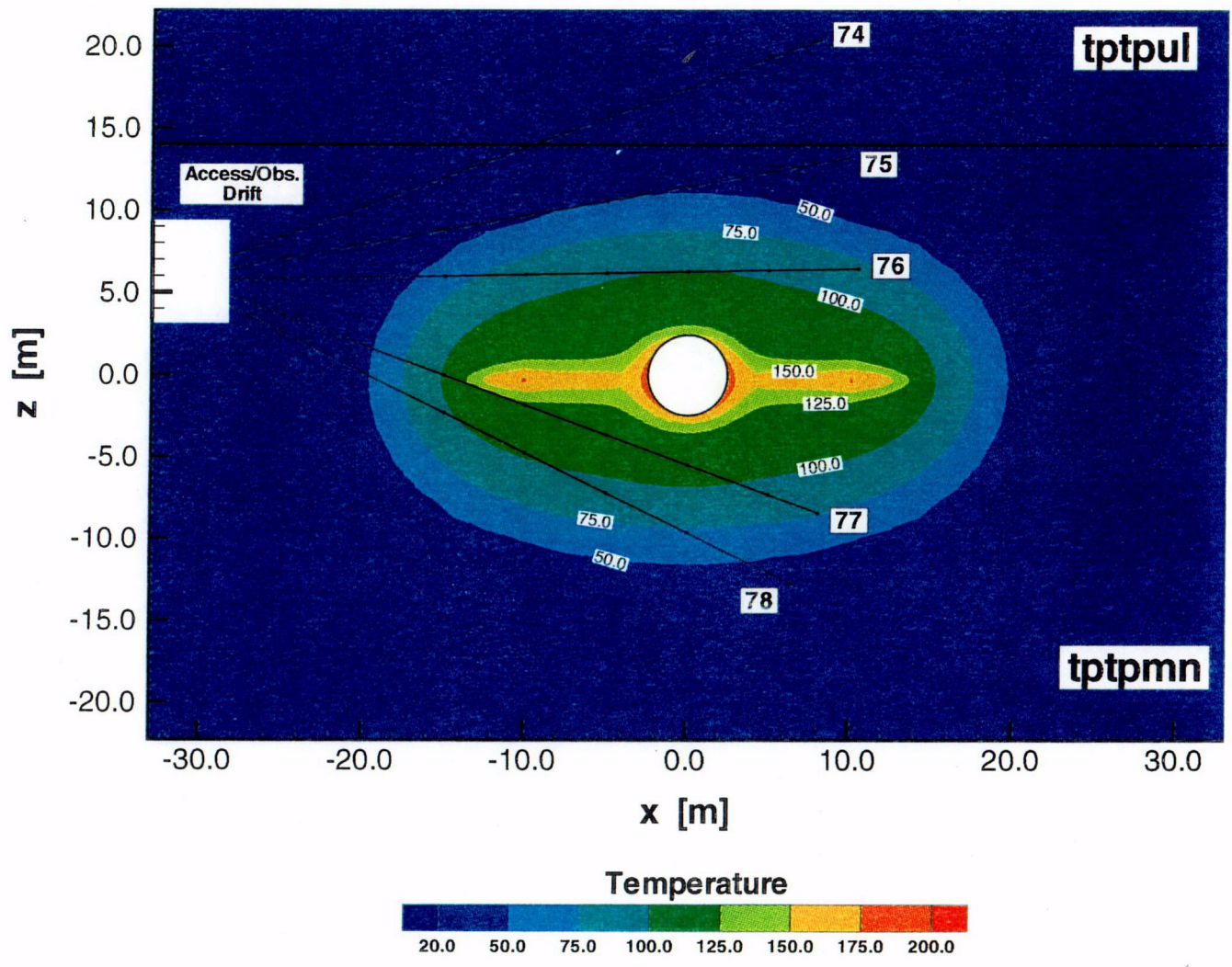


Figure 5.1-5 Temperature response after 1 year of heating in yz-cross section at  $x = 0.0$  m for 3.6 mm/yr infiltration case (1 year heating at 100%, 3 years heating at 50%).



**Figure 5.1-4** Temperature response after 1 year of heating in xz-cross section at  $y=30.18$  m for 3.6 mm/yr infiltration case (1 year heating at 100%, 3 years heating at 50%). Also presented is the location of hydrology holes 74 through 77.

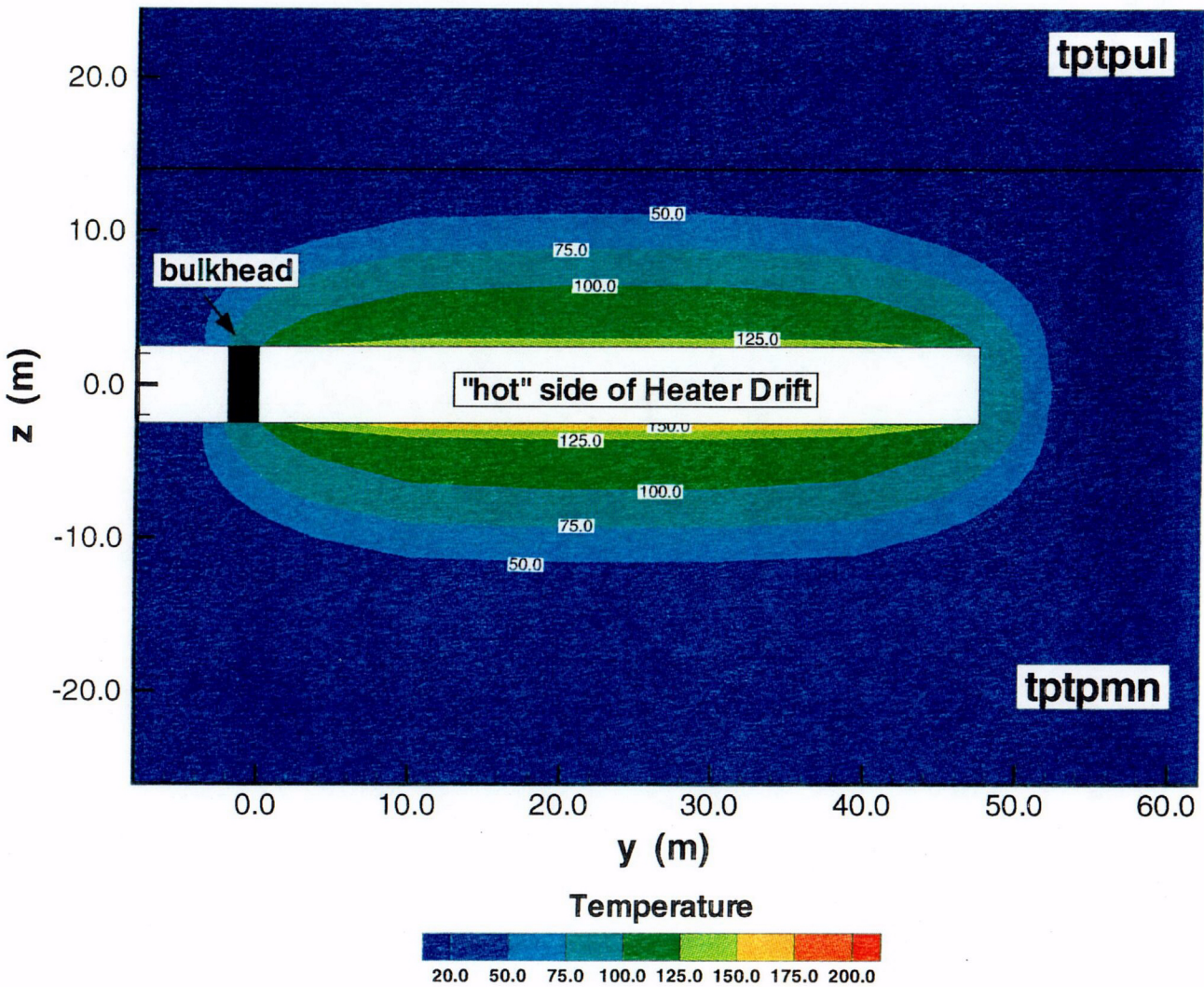


Figure 5.1-5 Temperature response after 1 year of heating in yz-cross section at  $x = 0.0$  m for 3.6 mm/yr infiltration case (1 year heating at 100%, 3 years heating at 50%).

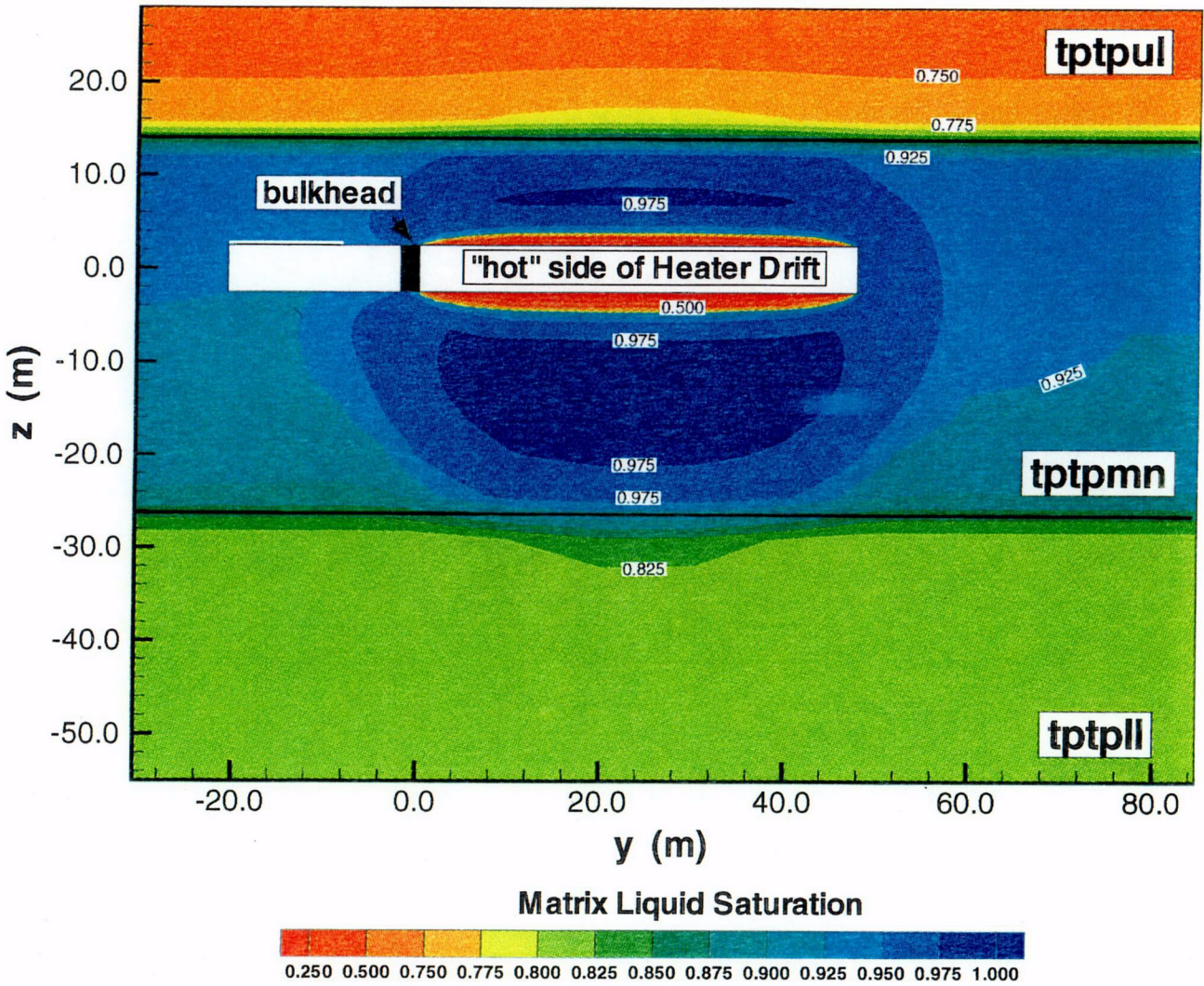
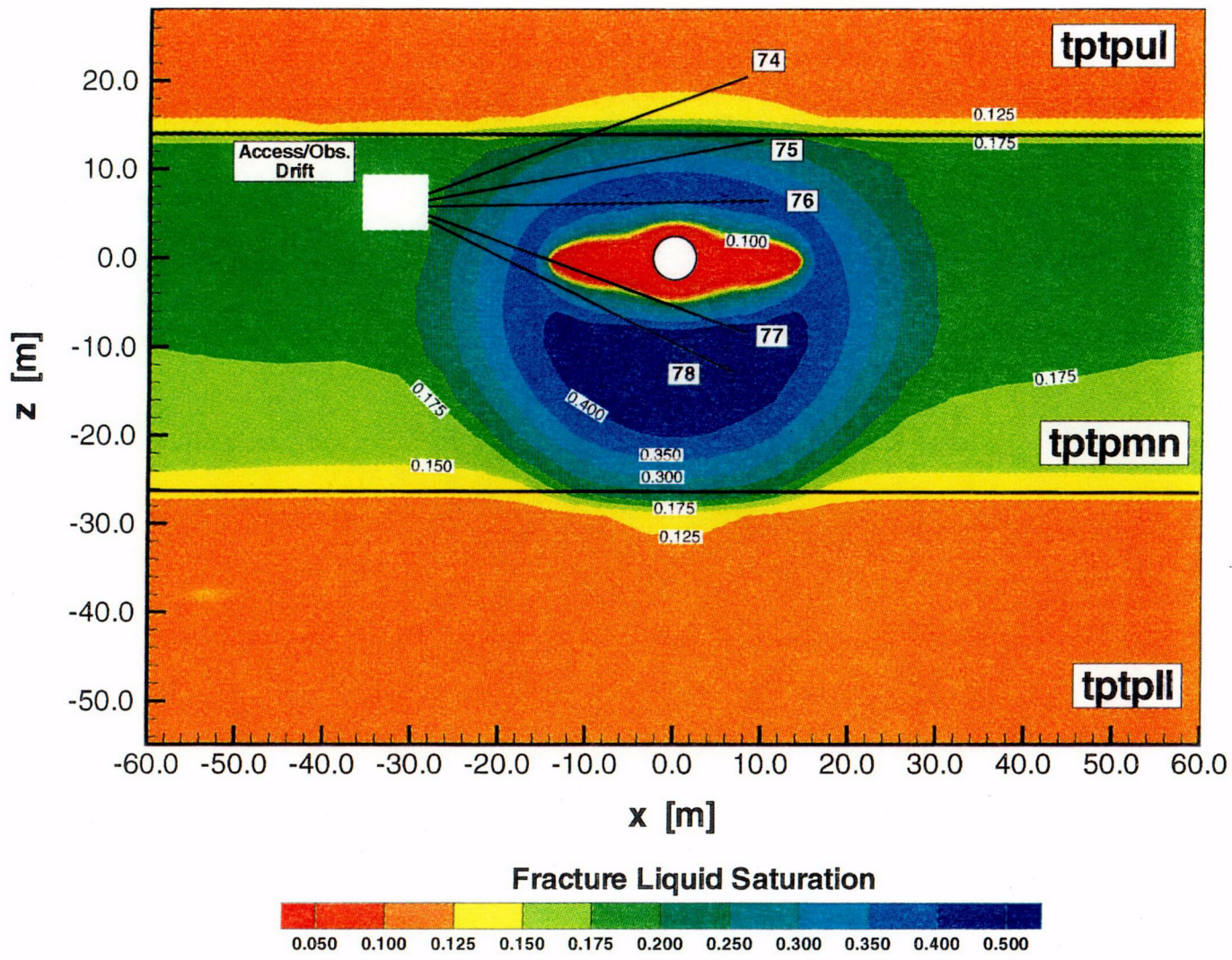


Figure 5.1-7 Matrix liquid saturation after 1 year of heating in yz-cross section at  $x = 0.0$  m for 3.6 mm/yr infiltration case (1 year heating at 100%, 3 years heating at 50%).



**Figure 5.1-8** Fracture liquid saturation after 1 year of heating in xz-cross section at y=30.18 m for 3.6 mmyr infiltration case (1 year heating at 100%, 3 years heating at 50%). Also presented is the location of hydrology holes 74 through 77.

C-05

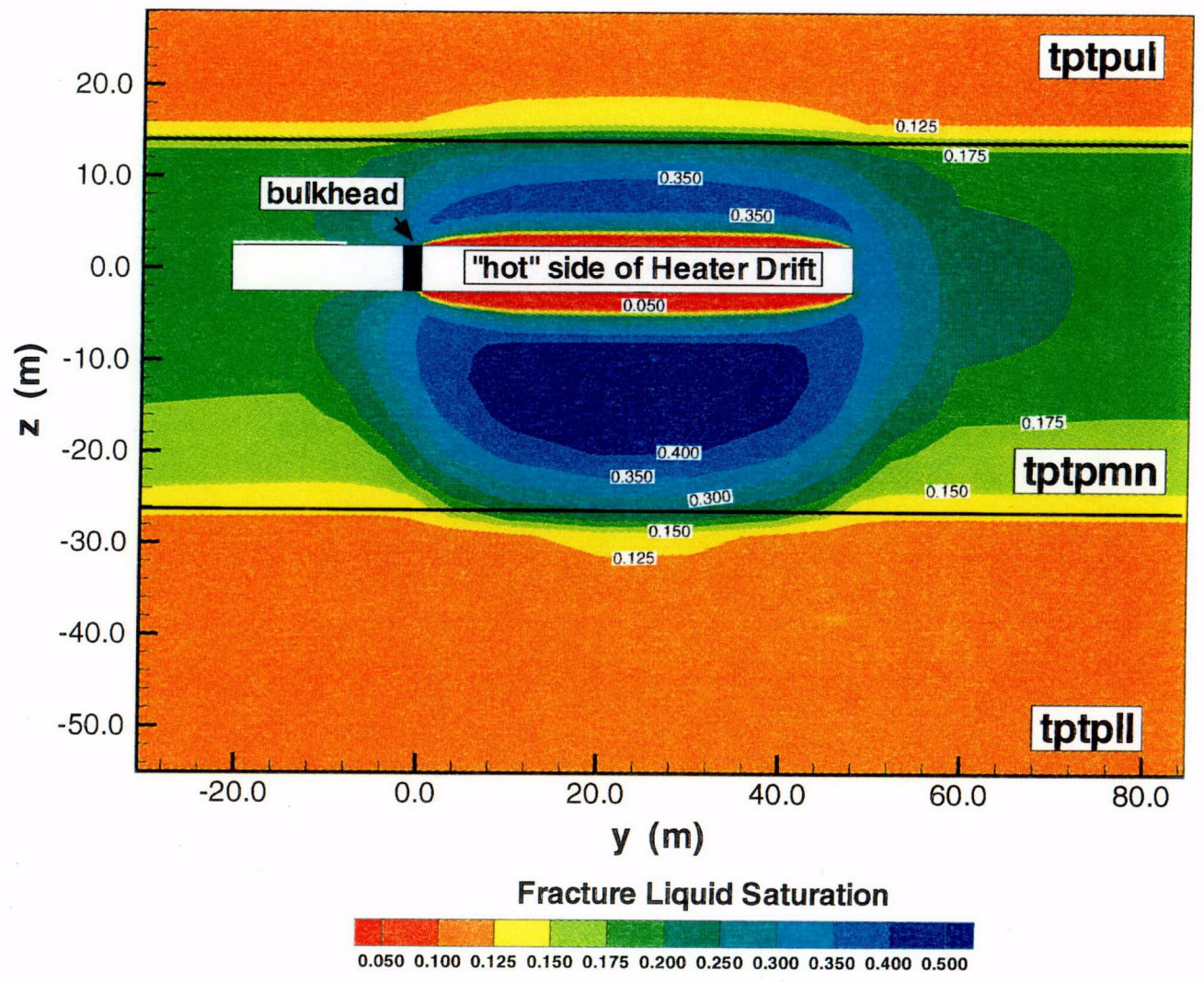


Figure 5.1-9 Fracture liquid saturation after 1 year of heating in yz-cross section at  $x = 0.0$  m for 3.6 mm/yr infiltration case (1 year heating at 100%, 3 years heating at 50%).

C-06

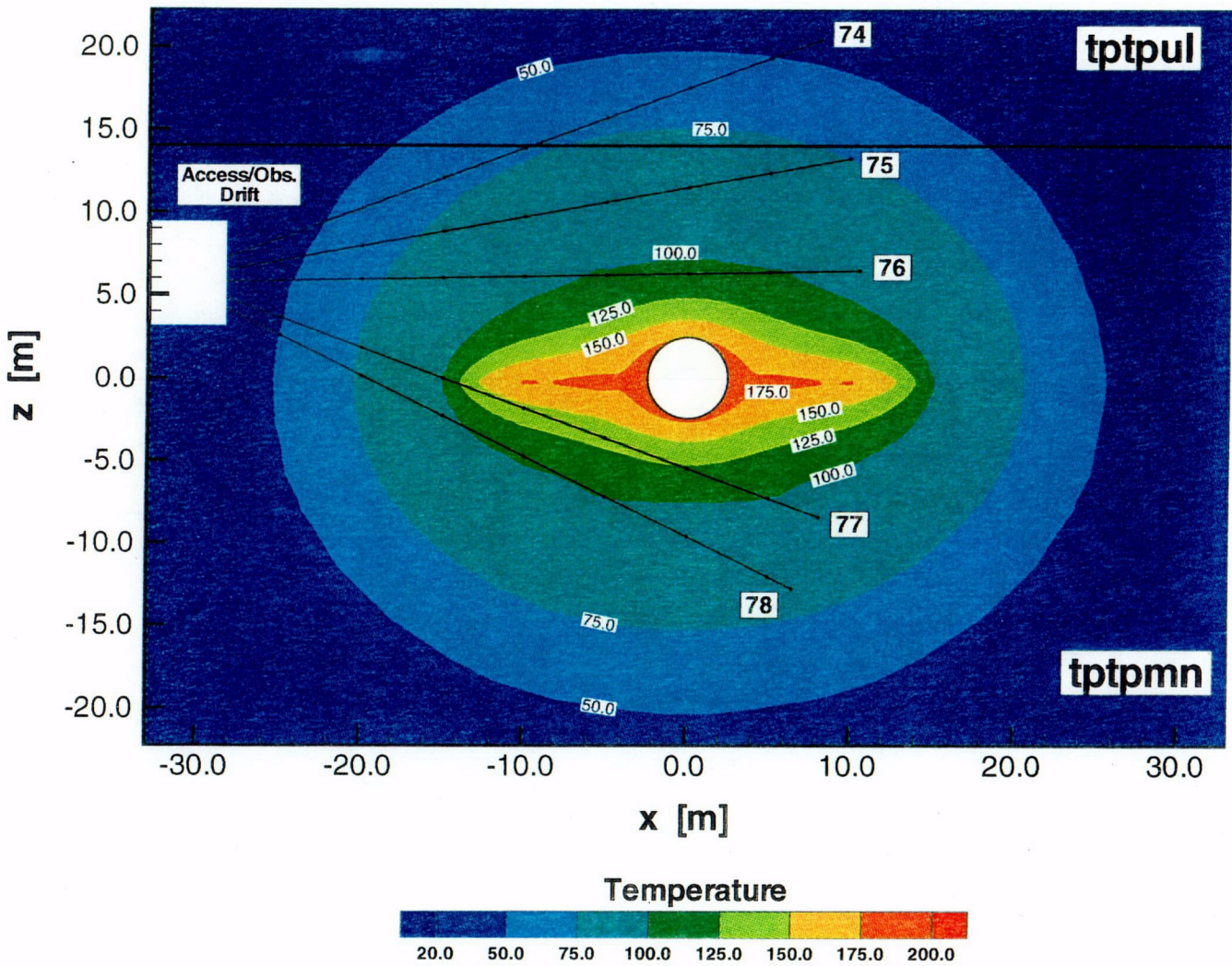


Figure 5.1-10 Temperature response after 4 years of heating in xz-cross section at y=30.18 m for 3.6 mm/yr infiltration case (1 year heating at 100%, 3 years heating at 50%). Also presented is the location of hydrology holes 74 through 77.

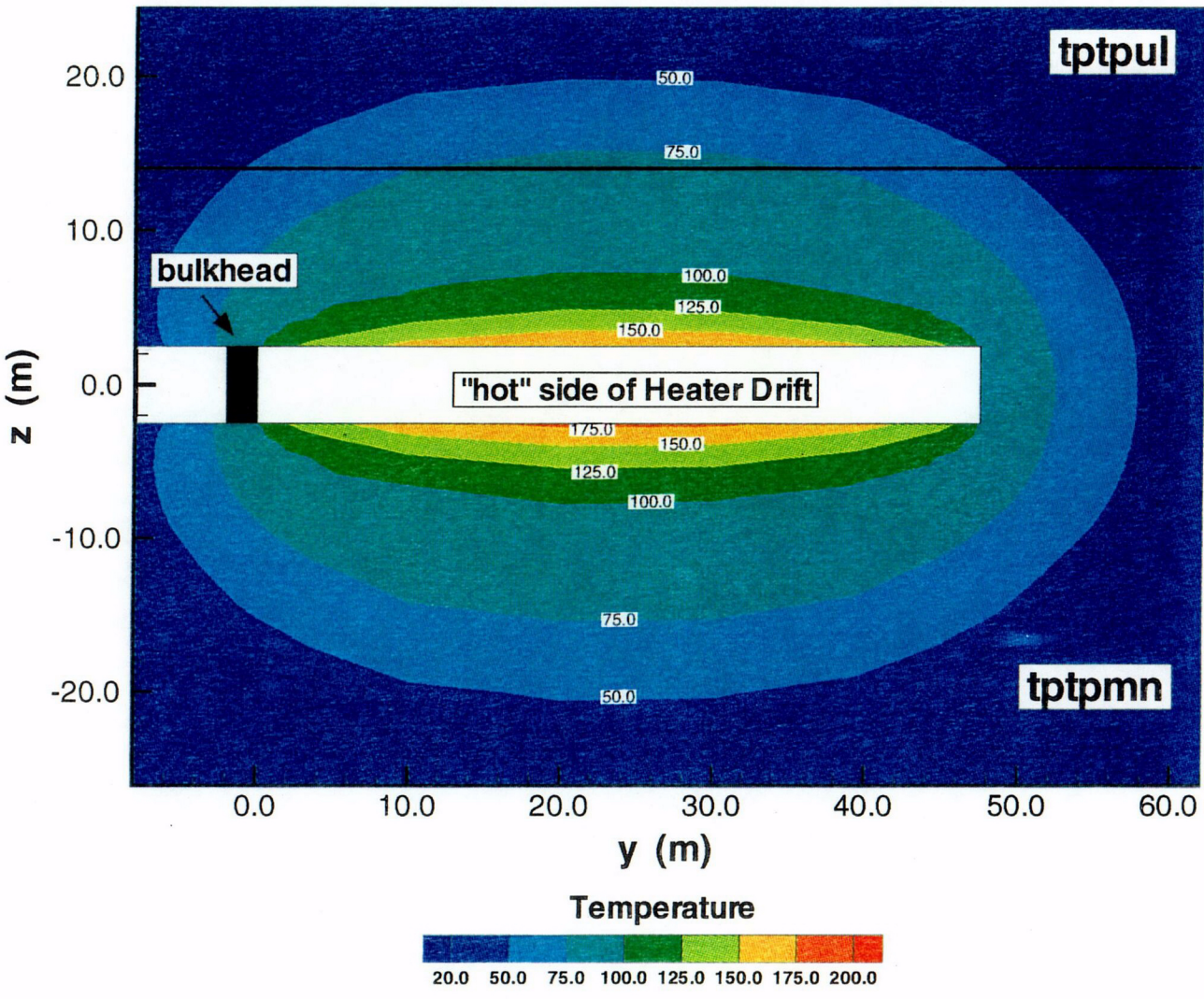
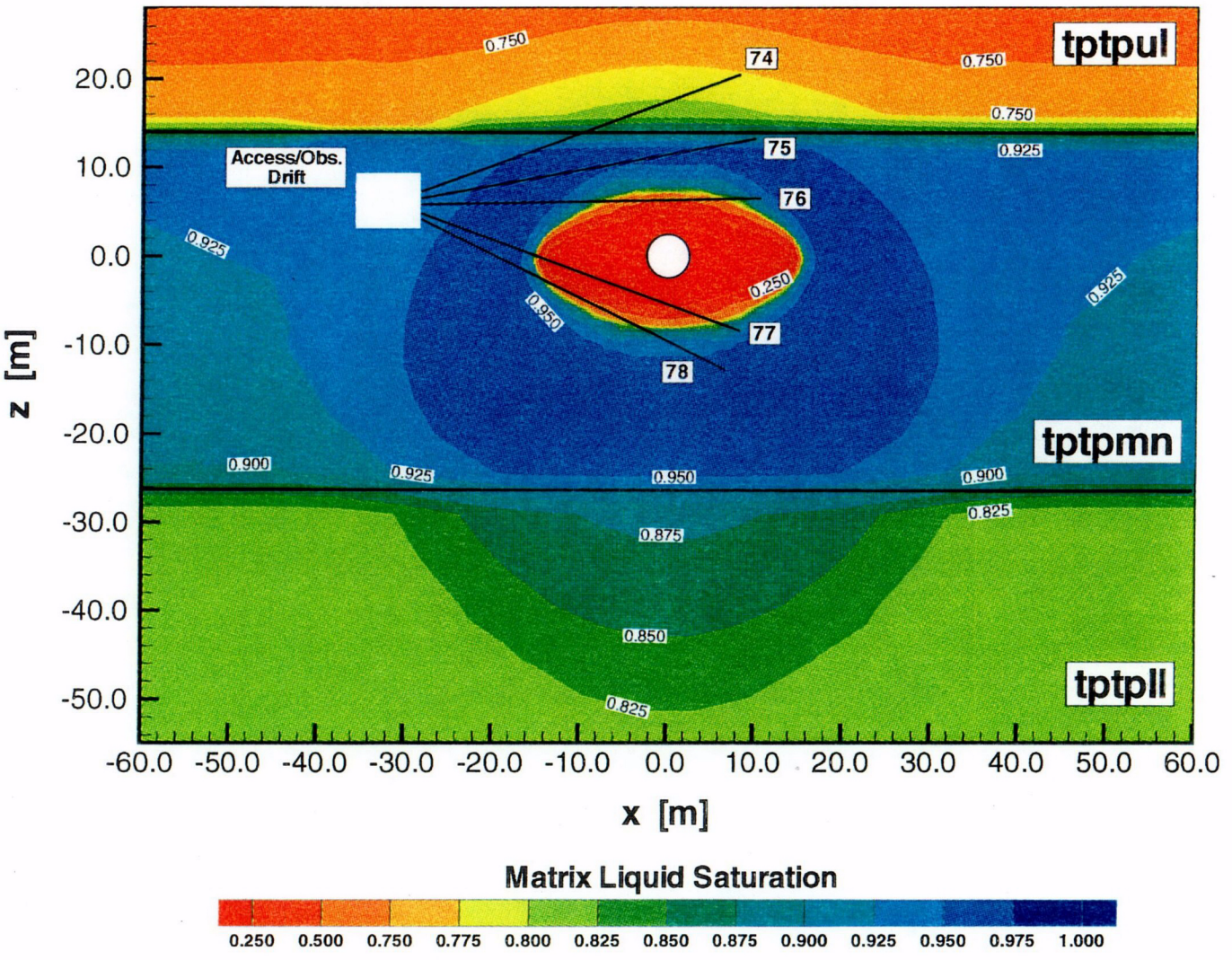


Figure 5.1-11 Temperature response after 4 years of heating in yz-cross section at x = 0.0 m for 3.6 mm/yr infiltration case (1 year heating at 100%, 3 years heating at 50%).

C-08



**Figure 5.1-12** Matrix liquid saturation after 4 years of heating in xz-cross section at  $y=30.18$  m for 3.6 mm/yr infiltration case (1 year heating at 100%, 3 years heating at 50%). Also presented is the location of hydrology holes 74 through 77.

C-09

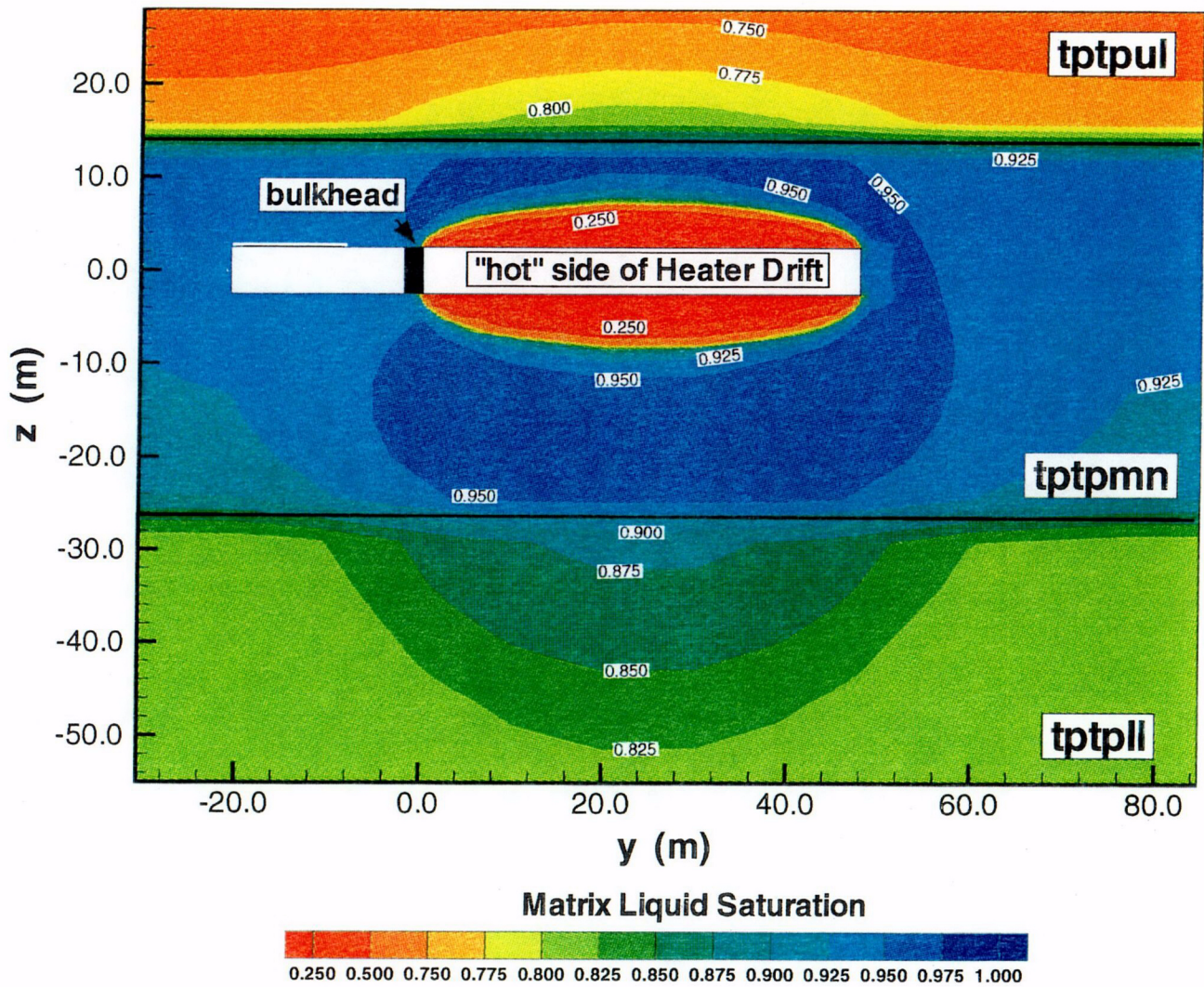
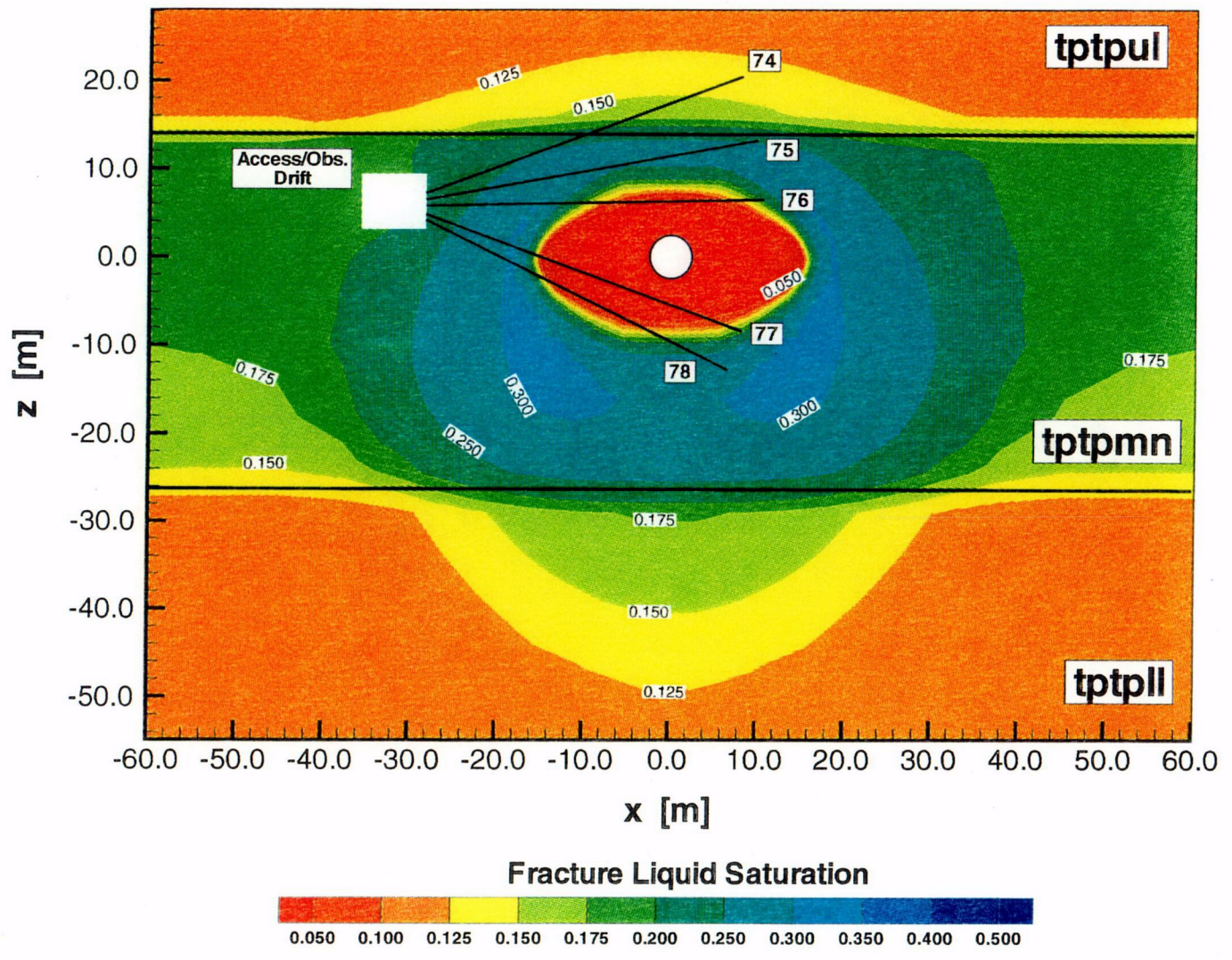


Figure 5.1-13 Matrix liquid saturation after 4 years of heating in yz-cross section at  $x = 0.0$  m for 3.6 mm/yr infiltration case (1 year heating at 100%, 3 years heating at 50%).



**Figure 5.1-14** Fracture liquid saturation after 4 years of heating in xz-cross section at y=30.18 m for 3.6 mm/yr infiltration case (1 year heating at 100%, 3 years heating at 50%). Also presented is the location of hydrology holes 74 through 77

0-11

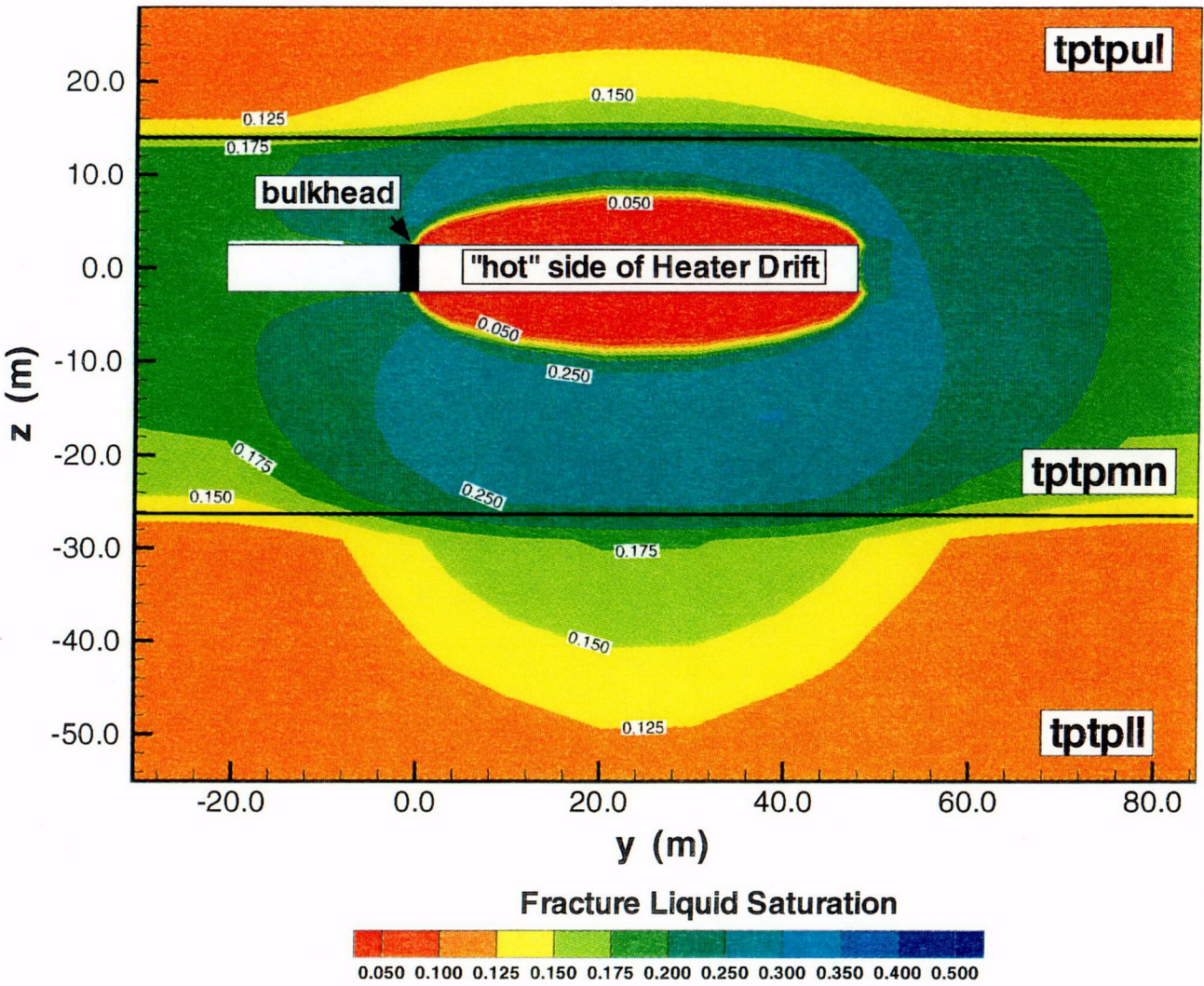


Figure 5.1-15 Fracture liquid saturation after 4 years of heating in yz-cross section at  $x = 0.0$  m for 3.6 m/yr infiltration case (1 year heating at 100%, 3 years heating at 50%).